

THESIS FOR THE DEGREE OF DOCTOR OF PHILOSOPHY

Optical remote sensing of industrial gas emission fluxes

John Johansson



CHALMERS

Department of Earth and Space Sciences
CHALMERS UNIVERSITY OF TECHNOLOGY
Göteborg, Sweden 2016

Optical remote sensing of industrial gas emission fluxes
JOHN JOHANSSON
ISBN 978-91-7597-316-6

© JOHN JOHANSSON, 2016

Doktorsavhandlingar vid Chalmers Tekniska Högskola
Ny serie nr. 3997
ISSN 0346-718X

Department of Earth and Space Sciences
Chalmers University of Technology
SE-412 96 Göteborg, Sweden
Phone: +46 (0)31-772 1000

Printed in Sweden
Chalmers Reproservice
Göteborg, Sweden 2016

Contact information:

John Johansson
Department of Earth and Space Sciences
Chalmers University of Technology
Hörsalsvägen 11
SE-412 96 Göteborg, Sweden

Phone: +46 (0)31-772 5655
Fax: +46 (0)31-772 3663
Email: john.johansson@chalmers.se

Last updated on January 4, 2016.



This work is licensed under the *Creative Commons Attribution 3.0 License*.

Typeset in \LaTeX

Optical remote sensing of industrial gas emission fluxes

John Johansson

*Optical Remote Sensing, Department of Earth and Space Sciences
Chalmers University of Technology*

Thesis for the degree of Doctor of Philosophy

Abstract

Mobile optical remote sensing techniques offer promising possibilities to quantify and geographically attribute local industrial gaseous emissions to the atmosphere. Studies have shown that such emissions are often poorly understood, underestimated, and thereby not properly accounted for in emission inventories and regional atmospheric chemistry models, especially for emissions of VOCs. A better understanding and quantification of industrial VOC emissions is crucial for combating ground-level ozone, a serious problem facing most of the world's larger urban areas.

This thesis presents results from a number of measurement campaigns primarily conducted in the area around Houston, Texas, USA, which has one of the world's largest concentrations of oil, gas and petrochemical industries. In the campaigns, the two flux measurement methods Solar Occultation Flux (SOF) and Mobile DOAS were used to quantify emissions of VOCs (alkanes and alkenes), SO_2 , NO_2 , and formaldehyde (HCHO) from the largest industrial conglomerates in the area.

Measured emissions are compared to industry estimates reported to emission inventories, showing discrepancies of up to an order of magnitude for VOCs but not for SO_2 and NO_2 . Emission factor models are used to estimate effects on VOC emissions of unrepresentative meteorological conditions during the measurement campaigns. These effects are determined to be too small to explain the discrepancies between measurements and reported emissions seen for VOCs.

A plume chemistry model is applied to a number of cases where formaldehyde were detected together with significant amounts of alkenes in order to assess whether the formaldehyde could be explained as a secondary pollutant from the oxidation of alkenes. The results of the modeling shows that secondary emissions can only explain a small fraction of the measured formaldehyde flux in most cases, suggesting that most of the formaldehyde emissions measured from local sources were primary emissions. Secondary emissions are, however, still believed to be the largest source of formaldehyde further downwind from sources.

Mobile multi-axis DOAS measurements of absolute vertical columns of NO₂ and HCHO were performed in the Houston Ship Channel as a part of the 2013 NASA DISCOVER-AQ campaign in Houston. An improved methodology for deriving the vertical columns from the measured slant columns is suggested and used. The measurements are compared to several other measurement methods employed in the campaign and a significant level of agreement is found.

Keywords: optical remote sensing, absorption spectroscopy, solar occultation, FTIR, DOAS, VOC, formaldehyde, gas emission, flux measurement

List of appended papers

This thesis is a summary of the following three papers. References to the papers will be made using roman numerals.

Paper I – J. Mellqvist, J. Samuelsson, **J. K. E. Johansson**, C. Rivera, B. Lefer, S. Alvarez, J. Jolly,
Measurements of industrial emissions of alkenes in Texas using the solar occultation flux method,
Journal of Geophysical Research, vol. 115, no. D17, p. D00F17, 2010

Paper II – **J. K. E. Johansson**, J. Mellqvist, J. Samuelsson, B. Offerle, J. Moldanova, B. Rappenglück, B. Lefer, J. Flynn,
Quantitative measurements and modeling of industrial formaldehyde emissions in the Greater Houston area during campaigns in 2009 and 2011,
Journal of Geophysical Research, vol. 119, no. 7, p. 4303–4322, 2014

Paper III – **J. K. E. Johansson**, J. Mellqvist, J. Samuelsson, B. Offerle, B. Lefer, B. Rappenglück, J. Flynn, G. Yarwood,
Emission measurements of alkenes, alkanes, SO₂ and NO₂ from stationary sources in Southeast Texas over a 5 year period using SOF and mobile DOAS,
Journal of Geophysical Research, vol. 119, no. 4, p. 1973–1991, 2014

Paper IV – **J. K. E. Johansson**, J. Mellqvist, B. Lefer, L. Judd,
Mobile MAX-DOAS measurements of NO₂ and HCHO during the 2013 DISCOVER-AQ campaign in Houston,
(manuscript in preparation), 2016

Other contributions (not included)

This is a list of conference contributions and scientific reports.

- A – J. Mellqvist, **J. K. E. Johansson**, J. Samuelsson, C. Rivera, B. Lefer, S. Alvarez,
Comparison of Solar Occultation Flux measurements to the 2006 TCEQ emission inventory and airborne measurements for the TexAQS II, *TERC report project H53, 2008*,
http://www.tceq.texas.gov/assets/public/implementation/air/am/contracts/reports/da/20081108-comparison.solar_occultation_flux_measurements.pdf
- B – J. Mellqvist, **J. K. E. Johansson**, J. Samuelsson, B. Offerle, B. Rappenglück, C.-S. Wilmot, R. Fuller,
Investigation of VOC radical sources in the Houston area by the Solar Occultation Flux (SOF) method, mobile DOAS (SOF-II) and mobile extractive FTIR ,
TERC report project H-102, 2010,
<http://files.harc.edu/Projects/AirQuality/Projects/H102/H102FinalReport.pdf>
- C – **J. K. E. Johansson**, J. Mellqvist, J. Samuelsson, B. Offerle, B. Rappenglück,
Investigation of VOC radical sources in the Houston Area by the Solar Occultation Flux (SOF) method and Mobile DOAS,
AGU Conference 2010, (poster), San Fransisco, CA, USA
- D – **J. K. E. Johansson**, J. Mellqvist, J. Samuelsson, B. Offerle, B. Rappenglück, D. Anderson, B. Lefer, S. Alvarez, J. Flynn,
Quantification of industrial emissions of VOCs, NO₂ and SO₂ by SOF and Mobile DOAS,
AQRP report project 10-006, 2011,
<http://aqrp.ceer.utexas.edu/projectinfo/10-006/10-006%20Final%20Report.pdf>
- E – **J. K. E. Johansson**, J. Mellqvist, B. Lefer, J. Flynn,
SOF HRVOC emission study at Longview, Texas,
NETAC report, 2012,
http://www.etcog.org/UserFiles/File/NETAC/NETAC_SOF_rev.pdf
- F – **J. K. E. Johansson**, J. Mellqvist, J. Samuelsson, B. Offerle, P. Anderson, B. Lefer, J. Flynn, Z. Sun,
Quantification of industrial emissions of VOCs, NO₂ and SO₂ by SOF and Mobile DOAS during DISCOVER-AQ,
AQRP report project 13-005, 2013,
http://aqrp.ceer.utexas.edu/projectinfoFY12_13%5C13-005%5C13-005%20Final%20Report.pdf

- G – **J. K. E. Johansson**, J. Mellqvist, P. Andersson, B. Lefer, J. Flynn
,L. Judd,
Analysis of VOC, NO₂, SO₂ and HCHO data from SOF, mobile DOAS and
MW-DOAS during DISCOVER-AQ,
AQRP report project 14-007, 2014,
[http://aqrp.ceer.utexas.edu/projectinfoFY14_15%5C14-007%5C14-007%20Final%20Report.](http://aqrp.ceer.utexas.edu/projectinfoFY14_15%5C14-007%5C14-007%20Final%20Report.pdf)
pdf

Acknowledgements

I would like to start by taking the opportunity to express my sincere gratitude to all the people, without whom the work behind this thesis would not have been possible, or at least not as rewarding. Although listing everybody would be impractical, the following people deserve a special mention.

All the colleagues in the Optical remote sensing group, for their help with instruments, theoretical questions, computer issues, and for sharing their knowledge and experience. Among them, especially my supervisor Professor Johan Mellqvist, for organizing field studies, for teaching me about spectroscopy and atmospheric science, and for together with me writing the papers included in this thesis and performing the measurements and data analysis that they are based on.

My second set of colleagues at Fluxsense AB, for keeping the knowledge about SOF measurements active between the research campaigns, and for teaching it to me over and over again. Special thanks to Jerker Samuelsson and Brian Offerle, who have participated and played major roles in all of the measurement campaigns which this thesis is based on.

All the people at the University of Houston who have participated in the measurements, for their assistance and patience. Especially Dr. Barry Lefer and Dr. Bernhard Rappenglück, for organizing the campaigns, and James Flynn, for custom building measurement vehicles and solving our technical problems.

Last but not ineluctably least, Andreas Skyman, for providing the Latex template for this thesis and for nitpickingly proofreading its content, ensuring that no person suffering from a low tolerance level for what he considers “unworthy usage of the language of Keats and Shelley” should come to harm at the hands of its author. Marcus Billeter and Ludde Edgren also deserve credit for providing the precursors to Andreas’s Latex template.

Table of contents

I Summary

1 Introduction	1
2 Atmospheric topics	3
2.1 Vertical structure of the atmosphere	3
2.1.1 Temperature	3
2.1.2 Pressure and density	5
2.1.3 Vertical transport times	7
2.2 Composition of the atmosphere	8
2.3 Atmospheric chemistry	9
2.3.1 Photochemical smog	10
2.4 Electromagnetic radiation in the atmosphere	14
2.4.1 Solar radiation	14
2.4.2 Molecular absorption	15
2.4.3 Rayleigh scattering	17
2.4.4 Scattering and absorption by aerosols	17
3 Optical remote sensing methods	19
3.1 Absorption spectroscopy	19
3.1.1 Instrument effects	20
3.1.2 Spectral fitting algorithms	23
3.2 Flux measurements	25
3.3 Solar Occultation Flux	29
3.3.1 Instruments	32
3.3.2 Spectral retrievals	35
3.4 Mobile DOAS	38
3.4.1 Instruments	38
3.4.2 Spectral retrievals	39
3.4.3 Radiative transfer modeling	41
3.5 Wind measurements	43
3.5.1 GPS radiosondes	43
3.5.2 Ground-based wind masts	44
3.5.3 Remote sensing wind profilers	45

3.6	Plume height estimation	47
3.7	Error analysis	51
3.7.1	Spectroscopic errors	51
3.7.2	Wind measurement errors	53
3.7.3	Other error sources	55
3.7.4	Composite flux measurement error	56
4	Summary of papers	59
4.1	Paper 1	59
4.2	Paper 2	60
4.3	Paper 3	62
4.4	Paper 4	64
5	Outlook	67
	Bibliography	69
II	Appended papers	75
	Paper I – Measurements of industrial emissions of alkenes in Texas using the solar occultation flux method	77
	Paper II – Quantitative measurements and modeling of industrial formalde- hyde emissions in the Greater Houston area during campaigns in 2009 and 2011	93
	Paper III – Emission measurements of alkenes, alkanes, SO ₂ and NO ₂ from stationary sources in Southeast Texas over a 5 year period using SOF and mobile DOAS	115
	Paper IV – Mobile MAX-DOAS measurements of NO ₂ and HCHO during the 2013 DISCOVER-AQ campaign in Houston	137

Part I

Summary

1

Introduction

In the 1940s a new form of air pollution phenomenon was first noticed in Los Angeles, California. While air pollution had certainly been a significant problem in the past, it had mainly been associated with the emissions of soot and sulfur dioxide from coal burning. In the modern world of the 1940s, coal was increasingly substituted for petroleum as the fossil fuel of choice. With the knowledge available at the time it may have seemed reasonable to assume that urban air quality problems would soon be a thing of the past. But instead it was discovered that evaporated hydrocarbons from the brave new petroleum-powered society, in combination with nitrogen oxides from combustion in automobiles and industries, could fuel a chemical process in the atmosphere that produced highly elevated concentrations of ground-level ozone, a strongly oxidizing agent that caused and aggravated respiratory diseases and led to destruction of vegetation and agricultural output. This process would later be termed *photochemical smog*.

Since then we have learned a lot more about the causes of photochemical smog and how it can be mitigated. At the same time, however, our societies have grown ever more dependent on petroleum for the purpose of transport and industrial production. Even if a lot of effort have been put into making sure that as little of that petroleum as possible evaporates into our atmosphere, no oil tank is airtight and even a very small fraction of a huge amount can still be plenty. Because of this, photochemical smog and its impact on our health and environment continues to be a significant concern in most cities around the world.

This thesis presents the results of several years of research aimed at quantifying industrial gas emissions of hydrocarbons (or the wider category known as *volatile organic compounds*) and other pollutants contributing to photochemical smog

by means of mobile ground-based remote sensing methods. This research has been conducted mainly in Houston, Texas and the surrounding region, which is the largest hub of the North American petroleum industry. Despite the focus on this particular region, we believe that many of the results have a more universal significance.

A short description of the structure of the thesis is given below:

- Chapter 2 provides very brief introductions to a number of atmospheric topics relevant to understanding the methods and results presented in subsequent chapters and the appended papers.
- Chapter 3 presents the theory and application of the the optical remote sensing methods used in the appended papers.
- Chapter 4 gives a short summary of each appended paper.
- Chapter 5 presents a brief outlook on possible future research.
- At the end of the thesis the four appended papers are presented in full versions.

2

Atmospheric topics

2.1 Vertical structure of the atmosphere

2.1.1 Temperature

The atmosphere of Earth is usually divided into a number of layers based on its thermal structure. Figure 2.1 shows an example of a typical vertical temperature profile of the atmosphere up to 120 km. The figure also shows the extent of the principal layers of the atmosphere: the *troposphere*, *stratosphere*, *mesosphere* and *thermosphere*. These are basically defined by the sign of the derivative of the temperature with respect to altitude (this derivative but with opposite sign is called the *lapse rate*). The reason for this classification is that this property to a large degree determines the patterns of circulation in the layers. A warmer air mass resting on top of a colder air mass is generally a stable configuration, i.e. it will remain intact in the absence of external forces, while the opposite configuration, a colder air mass resting on top of warmer, is generally unstable, i.e. the air masses will tend to mix and thereby smooth out the temperature gradient, unless it is upheld by external forces. Hence, the troposphere and the mesosphere, which have positive lapse rates, have significant vertical transport of air masses, while the stratosphere and the thermosphere, which have negative lapse rates (the temperature increases with altitude), have very little vertical transport. The boundaries between the layers are called the *tropopause*, *stratopause* and *mesopause*, and are defined by local minima and maxima of the temperature profile.

The main source of heating in the atmosphere is solar radiation and the characteristic temperature profile shown in figure 2.1 is caused by the way the radiation energy is transferred to the atmosphere. In the upper thermosphere, intense heating is supplied by ultraviolet (UV) light of very short wavelengths

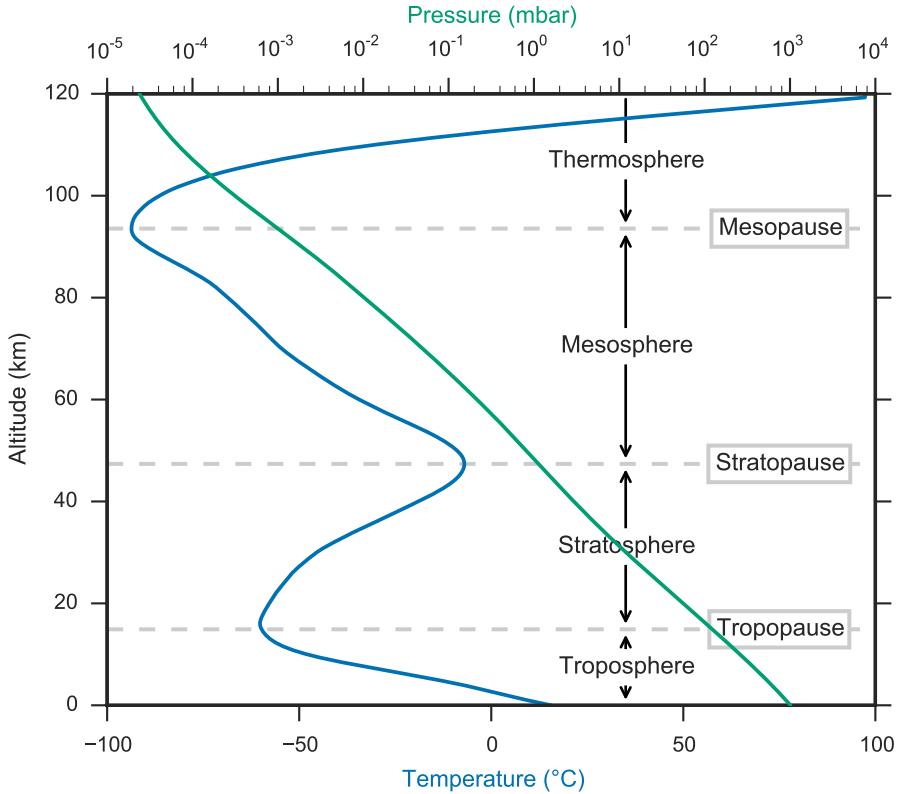


Figure 2.1: Average atmospheric temperature and pressure (at latitude 40° N) as a function of altitude and the extent of the principal layers of the atmosphere. Data taken from [1].

($\lesssim 200 \text{ nm}$) which is efficiently absorbed by molecular oxygen (O_2) and nitrogen (N_2). As you go further down through the atmosphere, less and less of this light will be available because of absorption by the air above and hence the temperature decreases. At the same time, however, the density of the atmosphere increases and with it the collision rate between its molecules. As the collision rate increases it becomes more and more likely for free oxygen (O) atoms created by photodissociation of O_2 to react with O_2 and form ozone (O_3). Ultraviolet light in the approximate wavelength range $200\text{--}300 \text{ nm}$ is far more efficiently absorbed by O_3 than by O_2 and hence the increase of O_3 , starting in the mesosphere, gives access to a source of heating not available to the layers above. As the O_3 fraction increases with decreasing altitude, the temperature increases again until you reach the stratopause, where the effect of decreasing availability of UV light becomes dominant also in the O_3 absorption wavelength range. Therefore the temperature starts decreasing again even though the O_3 fraction

continues to increase a bit into the stratosphere.

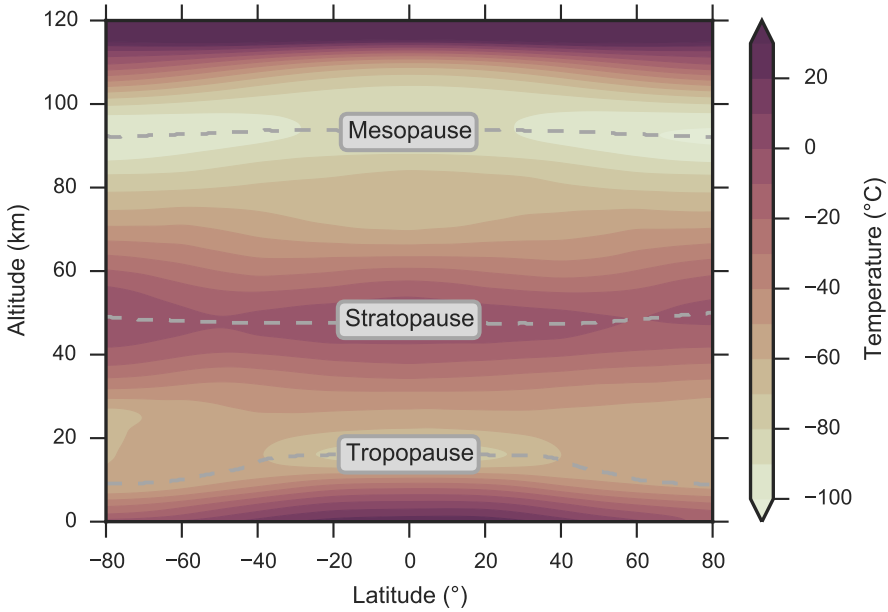


Figure 2.2: Average atmospheric temperature as a function of altitude and latitude. Data taken from [1].

Most of the light above approximately 320 nm and a bit into the infrared wavelength region passes through the whole atmosphere and is absorbed by the ground (although some of it is reflected). This causes very strong heating at ground level, which is transported up through the troposphere by means of convection, causing a very high positive lapse rate there. Due to convection the air parcels will expand and their water content will eventually condense, causing a characteristic lapse rate in the troposphere. The ground level heating is, however, unevenly distributed across the globe due to differences in solar irradiance. Figure 2.2 illustrates how the temperature varies with both altitude and latitude. This figure clearly shows that the higher solar irradiance around the equator causes a much higher tropopause (~ 17 km) than closer to the poles (~ 8 km). The altitudes of the stratopause and the mesopause on the other hand show no similarly strong dependence on latitude.

2.1.2 Pressure and density

To understand how the pressure and density of the atmosphere vary with altitude we can approximate the equation of state for a parcel of air with the ideal gas law

$$pV = NkT, \quad (2.1)$$

where p is the, V is the volume, k is the Boltzmann constant and T is the absolute temperature. Using this we can write the number density n , i.e. the number of molecules per volume unit, as

$$n \stackrel{\text{def}}{=} \frac{N}{V} = \frac{p}{kT}. \quad (2.2)$$

The mass density ρ is related to the number density by means of the average molar mass of the gas M and Avogadro's constant N_A and can hence be written

$$\rho = \frac{M}{N_A} n = \frac{M}{N_A kT} p = \frac{M}{RT} p. \quad (2.3)$$

In the last step $N_A kT$ has been substituted with the gas constant R . If a column of air is in hydrostatic equilibrium, i.e. it is experiencing no acceleration, the pressure at any point is caused only by the weight of the air above it. Hence the derivative of the pressure with respect to altitude z can be written

$$\frac{\partial p}{\partial z} = -\rho g, \quad (2.4)$$

where g is the local gravitational acceleration. Substituting (2.3) into (2.4) gives

$$\frac{\partial p}{\partial z} = -\frac{Mg}{RT} p. \quad (2.5)$$

This is a linear differential equation which can be solved by dividing by p , and integrating from ground level to z giving

$$\ln p(z) - \ln p(0) = - \int_0^z \frac{Mg}{RT} dz \quad \Rightarrow \quad p(z) = p(0) e^{- \int_0^z \frac{Mg}{RT} dz}. \quad (2.6)$$

Substituting this into (2.3) gives

$$\rho(z) = \frac{M}{RT} p(0) e^{- \int_0^z \frac{Mg}{RT} dz}. \quad (2.7)$$

According to (2.6) and (2.7), the pressure and density of the atmosphere decreases exponentially with altitude, although the scale of this exponential decay is not constant. The scale of the exponential decay is called the *scale height* H and is defined as

$$H = \frac{RT}{Mg}. \quad (2.8)$$

Over a height interval of this length, the pressure and density will decrease by a factor of e . In (2.8), T , M and g all have some variation with altitude, but in the altitude interval discussed so far (0–120 km), these variations are all moderate. Hence H at least has the same order of magnitude (5–9 km) throughout this interval. For this reason, the pressure profile approximates a straight line when plotted on a log scale, as seen in figure 2.1. Higher up in the thermosphere, however, H becomes much greater due to very high temperatures and decreasing M (which is due to gravitational separation of species by molecular mass at these altitudes). Since the depths of the layers discussed above are larger than the scale height at their altitude, it follows that each layer by mass constitutes a much larger fraction of the whole atmosphere than all the layers above it. The troposphere contains approximately 85% of the mass of the atmosphere, the stratosphere approximately 15%, the mesosphere approximately 0.1% and the thermosphere approximately 0.002%.

2.1.3 Vertical transport times

In most of the troposphere, large scale wind fields are primarily determined by a balance between pressure gradient forces and the Coriolis effect. This is called *geostrophic* wind and is characterized by air masses moving along isobars while circling high- or low-pressures. Close to ground level, however, the wind field deviates from geostrophic wind due to friction between the moving air masses and the ground, which causes turbulence. The layer closest to ground where the wind significantly deviates from geostrophic wind is called the *planetary boundary layer* (PBL) while the rest of the troposphere above it is called the *free troposphere*. The PBL is typically 1–3 km thick and the turbulence in it causes air masses from ground level to be vertically transported significantly faster within it than within the layers above it.

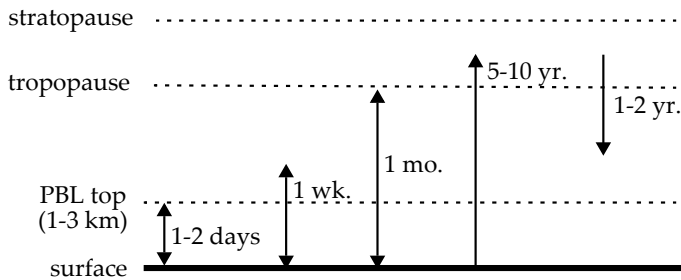


Figure 2.3: Characteristic time scales for vertical transport. Adapted from [2].

Figure 2.3 illustrates the characteristic time scales for which air masses from ground level are mixed up to different height layers. Mixing within the PBL typically take place on the time scale of a day or two, but during sunny conditions over land, the intense solar heating causes strong convection which can bring the mixing time down to less than an hour. This is in stark contrast to transport up to the stratosphere, which takes many years on average. Since most gas emissions to the atmosphere takes place at ground level, these large differences in time scales play a crucial role for which gas species and which types of chemical processes occur at different altitudes.

2.2 Composition of the atmosphere

The two overwhelmingly dominant molecular species in the atmosphere are molecular nitrogen (N_2) and oxygen (O_2), constituting approximately 78 % and 21 % of all atmospheric molecules respectively. All other gases in the atmosphere are collectively known as *trace gases*, each constituting less than 1 % of the total atmosphere. The 9 most abundant species (excluding water) and their mixing ratios are listed in table 2.1. Here we can see that the most abundant trace gases are the noble gases argon Ar, neon Ne, helium He and krypton Kr, and the greenhouse gases carbon dioxide CO_2 and methane CH_4 . Water vapor H_2O is not included in this listing since its atmospheric concentration is more variable.

Table 2.1: Average volume mixing ratios of the most abundant molecular species in the (dry) atmosphere. Adapted from [3] with CO_2 , CH_4 and N_2O updated based on [4].

Molecular species	Mixing ratio (ppmv)
Nitrogen (N_2)	780 789
Oxygen (O_2)	209 446
Argon (Ar)	9339
Carbon dioxide (CO_2)	398
Neon (Ne)	18.2
Helium (He)	5.24
Methane (CH_4)	1.83
Krypton (Kr)	1.14
Hydrogen (H_2)	0.5
Nitrous oxide (N_2O)	0.33

For N_2 and O_2 the mixing ratio is roughly constant throughout the atmosphere, but for many of the trace gases the concentration varies both with altitude, but also across the globe. Figure 2.4 shows the mixing ratios of a selection of important atmospheric constituents as functions of altitude. One important effect shaping these concentration profiles is the limited lifetimes of the species. Most trace gases are typically emitted into the atmosphere at ground level but will gradually over time react to form other species. If the average lifetime of a species is of the same order of magnitude as the time it takes for it to mix to the upper layers of the atmosphere, this will cause the concentration to decrease with

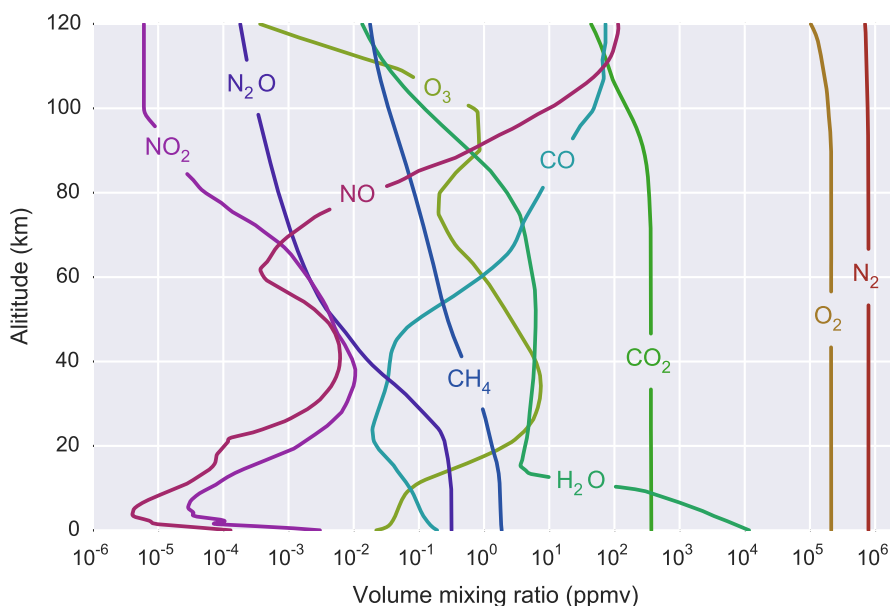


Figure 2.4: Average atmospheric volume mixing ratios as a function of altitude for selected molecular species. Data taken from [5].

height. This pattern is seen clearly for CH_4 and N_2O figure 2.4. As these species decrease with height due to reactions other may increase because they are formed from the same reactions. For instance NO_2 and NO_2 have very short lifetimes in the lower atmosphere and decrease in concentration very rapidly with height, but their abundance peak again in the stratosphere because they are formed as products from the degradation of N_2O . As we go further up into the atmosphere, more and more ultraviolet light becomes available causing photodissociation in some species. At the same time the atmosphere gets thinner, decreasing the likelihood of recombination of the dissociation products. This for instance causes the concentration of NO and CO to decrease in the upper atmosphere, while the concentration of NO_2 and CO_2 decrease. From approximately 100 km and above the atmosphere is so thin that the species start to separate with respect to molecular weight, with lighter species increasing in concentration with altitude and heavier species decreasing. This part of the atmosphere is called *heterosphere* as opposed to the *homosphere* below.

2.3 Atmospheric chemistry

Chemical reactions between the atmosphere's constituting species take place continuously as parts of a number of different processes. Although most of the atmosphere consist of long-lived species there are external drivers constantly

feeding these chemical processes. The two main drivers for chemical processes in the atmosphere may be thought of as the radiation from the sun and emissions of reactive species from the surface of the earth. The Chapman cycle, which is responsible for the ozone layer in the stratosphere, is an example of a chemical process caused entirely by ultraviolet solar radiation. The foundation of the Chapman cycle is the following four reactions [6]:



UV light with wavelengths below 250 nm cause photolysis (or photodissociation) of O_2 into free oxygen radicals (O) which can react with O_2 to form ozone (O_3), which can be turned back into O_2 either by photolysis or by reaction with O. After some time an equilibrium will be reached for which the reactions cancel each other out. The equilibrium concentration of O_3 will depend on the amount of UV radiation and the density of the atmosphere. At this point the process is cyclic, with no start and no final product, but without the radiation there would be no reactions and the high ozone levels in the stratosphere could not be as high as they are.

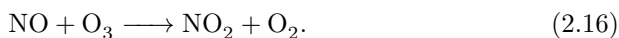
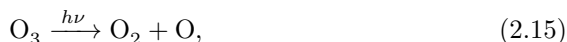
Chemical processes driven by emissions of reactive species on the other hand tend to be more linear, with the emitted species as the starting points, which through a number of reaction pathways is eventually turned into some final product species. Most major sources of gaseous emissions into the atmosphere can be classified as either anthropogenic (caused by humans), biogenic (caused by other biological entities), or volcanic. Anthropogenic emissions into the atmosphere have been linked to a number of different environmental problems, such as acidification, ozone depletion [7] and global warming [8].

2.3.1 Photochemical smog

Photochemical smog is a chemical process in the troposphere which is driven primarily by the emission of nitrogen oxides, or NO_x (the collective name for NO and NO_2), volatile organic compounds (VOCs), and solar radiation. Photochemical smog can cause highly elevated levels of ground-level ozone and other products that are associated with serious risks to human health, mainly in the form of respiratory diseases.

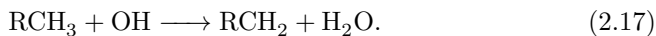
The most important reaction mechanisms are illustrated in figure 2.5. Since the short wavelength UV light that is the major source of ozone in the stratosphere

does not penetrate down to ground level, the major source of ozone in the troposphere is instead the photolysis of NO_2 . This photolysis only requires light of wavelengths below 430 nm, which reaches the troposphere in significant quantities during daytime, especially in clear conditions. In the presence of NO_x the tropospheric ozone concentration is largely governed by the following reactions:



These reactions are shown in the lower part of figure 2.5, where each species is represented by a box and the reactions are represented by arrows between the boxes. Here we can see how NO_x cycles back and fourth between NO_2 and NO , while oxygen cycles back and fourth between O_2 and O_3 . These two cycles are coupled through reaction (2.16). For a given set of photolysis rates and a given NO_x concentration, the concentrations of O_3 , O , NO_2 and NO will reach an equilibrium fairly quickly. Since an NO molecule is produced in the photolysis of NO_2 , together with each free O atom needed to produce O_3 , and since NO is so reactive with O_3 , equilibrium concentrations of O_3 can never reach particularly high levels in this system. To achieve higher ozone concentration reaction (2.16) needs to be by-passed by some other even faster reaction turning NO back to NO_2 , thereby decoupling the NO_x cycle from the O_2 – O_3 cycle, allowing continuous O_3 production without equally fast destruction by NO . In photochemical smog, this by-passing is the result of the oxidation of organic molecules.

Volatile Organic Compounds, or VOCs, is a term used to refer to organic molecules that are volatile enough at ambient temperatures to have significant evaporation, allowing them to play a role in atmospheric chemistry. Anthropogenic sources of VOCs are typically of greatest importance for photochemical smog, but biogenic sources can dominate in rural areas. Both industry and motor vehicles are large anthropogenic sources of VOC emissions, but the origin of the VOCs is generally oil and natural gas, regardless of the source. The most important oxidant for VOCs in the atmosphere is the hydroxyl radical, OH . In figure 2.5 a typical oxidation pathway of a typical VOC molecule, RCH_3 where R is an arbitrary carbon chain or other functional group, is illustrated. First the VOC molecule reacts with a hydroxyl radical:



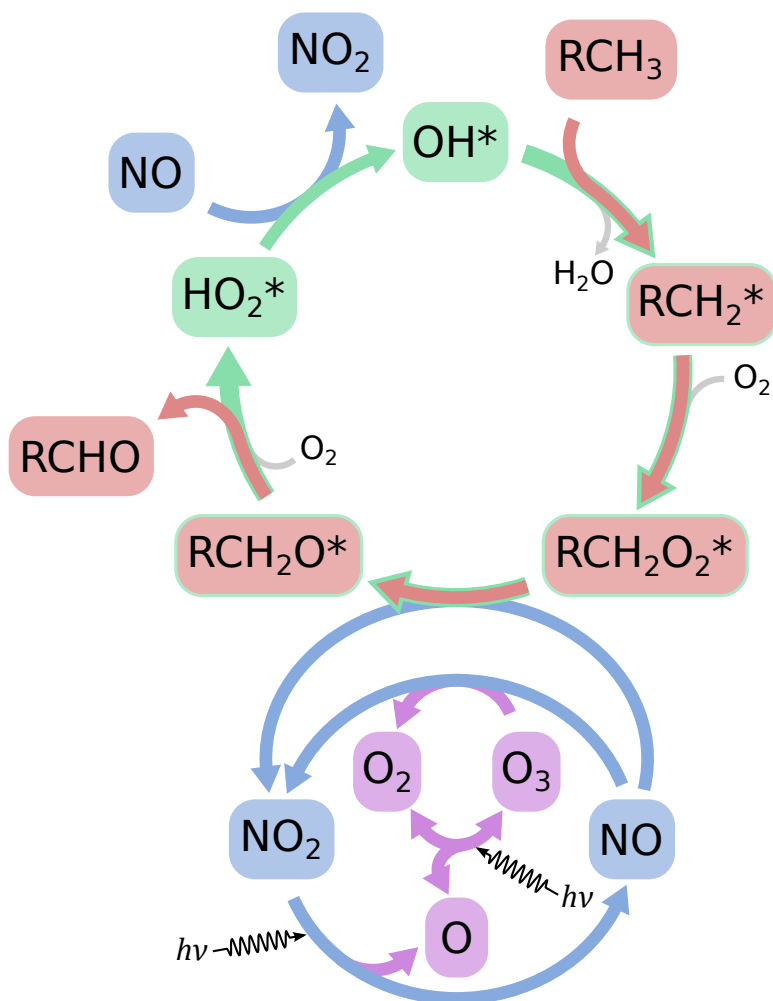
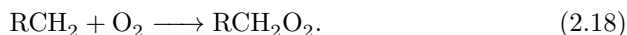
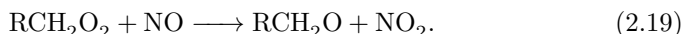


Figure 2.5: Illustration of the most fundamental reaction processes involved in photochemical smog. The reaction path for the partial oxidation of a volatile organic compound (VOC) is shown in red, the radical cycle is shown in green, the NO_x cycle is shown in blue and the oxygen-ozone cycle is shown in purple.

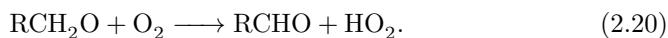
The hydroxyl radical takes a hydrogen atom from the VOC molecule, producing an organic radical and a water molecule. The organic radical then reacts with an oxygen molecule to form a peroxyradical:



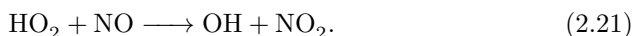
The peroxyradical reacts with an NO, which takes one oxygen atom to form NO₂, thereby bypassing the NO–O₃ reaction as explained above:



The resulting oxyradical reacts with an oxygen molecule, which takes a hydrogen atom and forms a hydroperoxyl radical, HO₂, and an aldehyde:



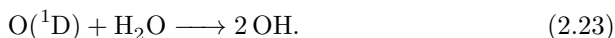
The hydroperoxyl radical reacts with another NO to form NO₂ and a hydroxyl radical, replacing the one consumed in the first oxidation step:



If the reactions (2.17)–(2.21) are combined, the resulting net reaction becomes:



Of course, far from all VOCs are on the form RCH₃, and even if they were, there are many other possible reaction paths than the one described here. However, the net reaction (2.22) still captures the general broad pattern for the oxidation of most VOCs pretty well. Hydrogen atoms on the VOCs are gradually replaced by oxygen atoms, while at the same time oxidizing NO to NO₂. The oxidation is dependent on OH radicals, but they are for the most part not consumed in the process. The total number of radicals (marked in green in 2.5) is conserved by most reaction steps in the oxidation process, but they cycle through the forms of hydroxyl radicals, hydroperoxyl radicals, and different forms of organic radicals. There are several sources of the hydroxyl radicals needed for oxidation of VOCs, but one of the most important is the photolysis of O₃. The free oxygen atom formed from this photolysis is in an excited state, O(¹D), which allows it to react with a water molecule to form two hydroxyl radicals:



This is one of several ways in which the photochemical smog chemistry generates the hydroxyl radicals needed to keep it going. There are of course also reactions causing losses of radicals, but the fact that the process creates its own radicals means that the necessary prerequisites for photochemical smog formation are just NO_x , VOCs and sun light. In terms of ground-level ozone formation, the NO_x and the sun light can be thought of as producing the ozone, while the VOCs prevent the ozone from being consumed as fast as it is produced. Even though these are the only prerequisites for photochemical smog, there are many other factors influencing the severity, most notably perhaps the meteorology.

Although all VOCs contribute to photochemical smog, alkenes are often of particular interest. Even though emissions of alkanes are typically much larger than alkene emissions, alkene can still dominate the ozone formation because they have higher OH reactivity. The higher OH reactivity of alkenes also gives them a typical lifetime that is better matched to the typical lifetime of NO_x . A polluted air mass may often run out of NO_x before much of the alkanes have had time to be oxidized. Alkenes are also involved in two of the other major ways in which photochemical smog produces its own hydroxyl radicals. One is through ozonolysis, in which alkenes react with ozone forming OH in varying amounts. The other way is through the production of formaldehyde (HCHO), which is produced in high yields from the oxidation of many alkenes. Photolysis of the formaldehyde results in the formation of HO_2 radicals, which in the presence of NO will be converted to OH through reaction (2.21). By contributing to the formation of OH, alkenes also speed up the oxidation of VOCs. Additionally, the production of OH from the photolysis of formaldehyde makes any primary emission sources of formaldehyde especially interesting. Primary emissions would make formaldehyde available early in the morning, before the photochemical smog has started, and the OH produced from its photolysis could speed up the photochemistry more rapidly.

2.4 Electromagnetic radiation in the atmosphere

2.4.1 Solar radiation

The major source of electromagnetic radiation, or light, in the visible and ultra-violet regions in the atmosphere is the sun. For the infrared spectral region sun light is still dominant in the near infrared, but as the wavelengths get longer, blackbody radiation from earth itself becomes more and more important. Most of the solar electromagnetic radiation that reaches earth originates from a region of the sun called the *photosphere*, which ranges in temperature between 4000 K and 8000 K [9]. The solar spectral radiance curve approximately matches the Planck function for a temperature of approximately 5800 K, which can be seen as an approximate average of the temperature in the photosphere. Figure 2.6 shows a plot of the solar spectral radiance as a function of wavelength. Although the sun's spectrum can be thought of as Planck function continuum on a coarse wavelength resolution, the high resolution spectrum is full of narrow lines where

the radiance is much lower. These lines are known as *Fraunhofer lines* and are caused by absorption of light in the solar layers above the photosphere, mainly the *chromosphere*. The fine structure caused by the Fraunhofer lines is illustrated on different scales in figure 2.6. The Fraunhofer lines tend to be more closely spaced in the ultraviolet region and less frequent in the infrared region.

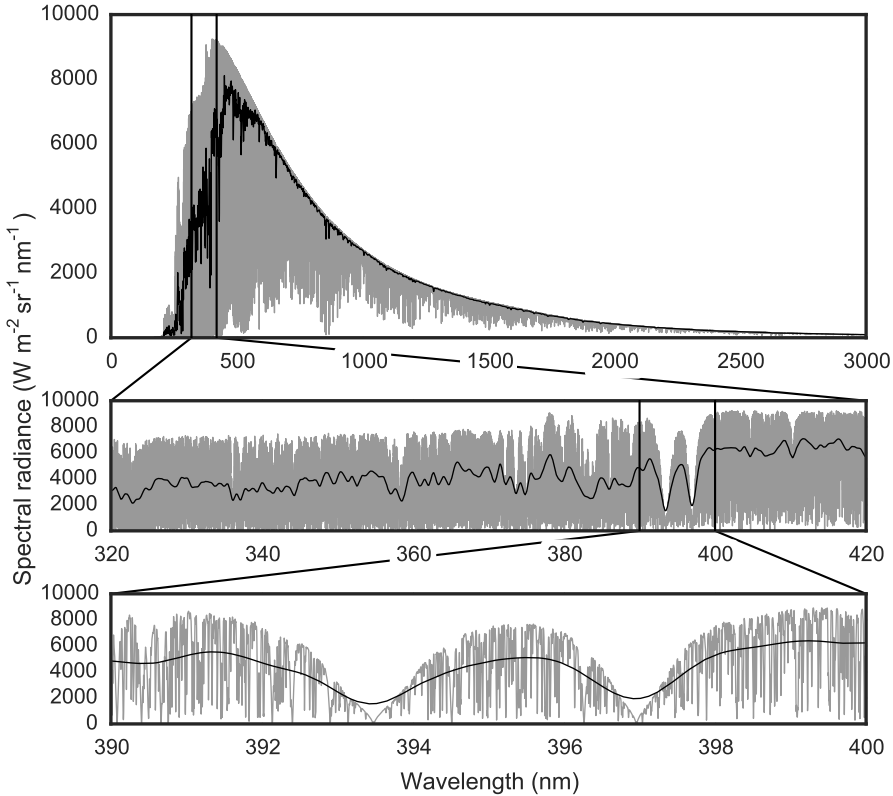


Figure 2.6: Spectral radiance of sun light before entering the atmosphere. A high resolution spectrum is shown in gray and a degraded version is shown in black. The lower panels show the fine structure on the spectrum in more narrow wavelength windows. Data taken from [10].

2.4.2 Molecular absorption

Absorption of electromagnetic radiation by molecules in the atmosphere depends fundamentally on the structure of the molecule. The energy of a molecule is the sum of its electronic energy, its vibrational energy and its rotational energy, each of which only can take quantized values associated with its possible electronic, vibrational and rotational states. Electromagnetic radiation of a certain frequency ν can only be absorbed by a molecule if its energy $h\nu$ matches

the difference in energy between the current state of the molecule and a state with a higher energy, thereby causing an excitation to the higher state. Absorption in the visible and UV regions, is generally due to an electronic excitation, which can be combined with vibrational and rotational transitions. Absorption in the infrared region is generally due to a vibrational excitation, which can be combined with a rotational transition. The energy needed for pure rotational transitions correspond to absorption in the microwave region. Each possible excitation for a molecule causes an absorption line in the absorption cross section for that species. The strength of each line depends on the likelihood of the excitation, which is a result of quantum mechanical selection rules for transition between states. The absorption cross section $\sigma(\nu)$ for a molecular species can be seen as a superposition of all these absorption lines:

$$\sigma(\nu) = \sum_i S_i n_i(T) f(\nu - \nu_i), \quad (2.24)$$

where S_i is the strength of the absorption line i , $n_i(T)$ is the population of the lower state of the transition, which is temperature dependent, ν_i is the central frequency of the line corresponding to the excitation energy, and $f(\Delta\nu)$ is a function describing the broadening of the line. There are two major effects that cause line broadening: Doppler broadening and pressure broadening. Doppler broadening causes a Gaussian lineshape $f_D(\Delta\nu)$:

$$f_D(\Delta\nu) = \frac{1}{\sqrt{\pi}} e^{-\frac{\Delta\nu^2}{\alpha_D^2}}, \quad (2.25)$$

where the Doppler broadening width α_D is given by:

$$\alpha_D = \nu_i \sqrt{\frac{2k_B T}{c^2 m}}, \quad (2.26)$$

where k_B is the Boltzmann constant, T is the temperature of the gas, c is the speed of light, and m is the molecular mass. Pressure broadening on the other hand causes a Lorentzian lineshape $f_P(\Delta\nu)$:

$$f_P(\Delta\nu) = \frac{\alpha_P}{\pi(\Delta\nu^2 + \alpha_P^2)}, \quad (2.27)$$

where the pressure broadening width α_P is given by:

$$\alpha_P = \alpha_0 \frac{p}{p_0} \left(\frac{T_0}{T} \right)^n, \quad (2.28)$$

where α_0 is the pressure broadening width for some reference pressure p_0 and temperature T_0 and n is an exponent that varies between 1/2 and 1 depending

on the molecule. The combined line broadening function $f(\Delta\nu_i)$ is given by the convolution of the Doppler and pressure broadening lineshapes:

$$f(\Delta\nu) = \int f_D(\Delta\nu') f_P(\Delta\nu - \Delta\nu') d\Delta\nu'. \quad (2.29)$$

The convolution of a Gaussian and a Lorentzian lineshape is called a Voigt profile. In the lower part atmosphere, approximately below 20 km, the pressure broadening of the line dominates the widths of the lines, while the Doppler broadening dominates from approximately 50 km and above [9].

2.4.3 Rayleigh scattering

Scattering of light by particles much smaller than the wavelength of the light is called Rayleigh scattering. For UV, visible and infrared light this is practically synonymous with molecular scattering. The Rayleigh scattering cross section $\sigma_r(\lambda)$ for a molecule can be expressed in terms of the polarizability of the molecule α as [9]:

$$\sigma_r(\lambda) = \frac{128\pi^5 \alpha^2}{3\lambda^4}. \quad (2.30)$$

The intensity of light scattered from one direction to another, I , in a spherical volume of radius r is given by:

$$I = I_0 \frac{\sigma_r}{r^2}(\lambda) \frac{P(\Theta)}{4\pi}, \quad (2.31)$$

where Θ is the angular difference between the incoming and scattered light, and $P(\Theta)$ is known as the phase function. The phase function for Rayleigh scattering of unpolarized light is given by [9]:

$$P(\Theta) = \frac{3}{4}(1 + \cos^2 \Theta). \quad (2.32)$$

As seen in equation (2.30), Rayleigh scattering is proportional to λ^{-4} which means that its significance varies greatly between different wavelength regions. In the UV region Rayleigh scattering is very strong, while in the infrared region it is often negligible.

2.4.4 Scattering and absorption by aerosols

For scattering of light by particles of similar or greater size than the wavelength, Rayleigh scattering theory is not applicable. For UV, visible and infrared light, this would apply for most common types of aerosols. Scattering and absorption of light by aerosols are often treated together since they are closely related. The

combined scattering and absorption of light by aerosols may be described by an extinction cross section $\sigma_e(\lambda)$, representing the sum of the absorption and scattering cross sections, a single scattering albedo ω , representing the ratio of the scattering cross section to the extinction cross section, and a phase function $P(\Theta)$ but analytical expressions with wide applicability can in general not be derived for these given the great variability and complexity in terms of size, composition, shape and structure of the aerosols. The absorption and scattering of light by an isotropic homogeneous sphere may be described by *Lorentz-Mie scattering* theory, but for many types of aerosols that is not a very good approximation. Many different methods to numerically calculate scattering and absorption properties of different types of aerosol exist but that is beyond the scope of this thesis.

In the general case, absorption and scattering by aerosols in the atmosphere vary more slowly with wavelength compared to molecular absorption and scattering. Aerosols do not exhibit the type of narrow band absorption signatures that molecular species have, nor the strong λ^{-4} proportional scattering.

3

Optical remote sensing methods

3.1 Absorption spectroscopy

The two main measurement techniques discussed in this thesis, Solar Occultation Flux (SOF) and Mobile Differential Optical Absorption Spectroscopy (Mobile DOAS), are both applications of absorption spectroscopy. Absorption spectroscopy is based on the property of many molecular species to absorb light in unique wavelength dependent patterns and on that the magnitude of this absorption is directly related to the quantity of gas that the light passes through. In the absence of other effects, the change in intensity of light due to molecular absorption as it passes through an air mass is described by the Beer–Lambert law:

$$I(\lambda) = I_0(\lambda) \exp \left(- \int_P \sum_i n_i(\mathbf{x}) \sigma_i(\lambda, T, p) d\mathbf{l} \right). \quad (3.1)$$

Here $I_0(\lambda)$ is the spectral radiance of the light as a function of wavelength λ before passing through the air mass and $I(\lambda)$ is the same quantity after having passed through the air mass. $n_i(\mathbf{x})$ is the number density of molecular species i at point \mathbf{x} and $\sigma_i(\lambda, T, p)$ is the absorption cross section of i at wavelength λ , which is also temperature and pressure dependent. The integral is a path integral over the path of the light, P , through the air mass and the sum is of all absorbing molecular species in the air mass.

In many applications, the spatial variation in the absorption cross sections along

the path, due to temperature and pressure variation, can be neglected. In that case, it can be noted that all the wavelength dependence in the exponential in (3.1) is due to $\sigma_i(\lambda, T, p)$, while all the spatial dependence is due to $n_i(\mathbf{x})$. This makes it convenient to define the path integrated number density of species i as S_i :

$$S_i = \int_P n_i(\mathbf{x}) d\ell. \quad (3.2)$$

This quantity is often called column, column density or column concentration. Using this definition, (3.1) can be written:

$$I(\lambda) = I_0(\lambda) \exp \left(- \sum_i S_i \sigma_i(\lambda) \right). \quad (3.3)$$

Here the temperature and pressure dependence of the absorption cross sections have been omitted. If we divide both sides of (3.3) by $I_0(\lambda)$, take the natural logarithm and multiply by -1 , we get:

$$- \log \left(\frac{I(\lambda)}{I_0(\lambda)} \right) = \sum_i S_i \sigma_i(\lambda). \quad (3.4)$$

The quantity on the left hand side of (3.4) is called optical density or absorbance. The basic principle of most absorption spectroscopy is to measure $I(\lambda)$ and $I_0(\lambda)$, calculate the absorbance, and based on known cross sections $\sigma_i(\lambda)$ find the values for S_i that satisfy (3.4). In many applications, it is not possible to measure $I_0(\lambda)$ directly, so instead a reference spectrum $I_r(\lambda)$, which has been affected by absorption by a different air mass, is used. The equivalent to (3.4) then becomes:

$$- \log \left(\frac{I(\lambda)}{I_r(\lambda)} \right) = \sum_i \Delta S_i \sigma_i(\lambda), \quad (3.5)$$

where ΔS_i is the difference in S_i for the two measurements. This is called a differential measurement and ΔS_i are called differential column densities.

3.1.1 Instrument effects

The spectral radiance $I(\lambda)$ can of course not be measured as an ideal continuous function of λ , but instead it is measured in a discrete number of wavelength channels. The instrument performing this measurement, a spectrometer, can be thought of as performing a transform from $I(\lambda)$ to a discrete vector I_j . In the general case, this transform is of the form:

$$I_j = \int w_j(\lambda) I(\lambda) d\lambda, \quad (3.6)$$

where $w_j(\lambda)$ is a weighting function for wavelength channel j . In most cases, the weighting functions can be assumed to be approximately of the form:

$$w_j(\lambda) = a(\lambda) f(\lambda - \lambda_j), \quad (3.7)$$

where $a(\lambda)$ is a slowly varying function describing the overall sensitivity of the instrument to a certain wavelength, λ_j is the center wavelength for channel j , and $f(\Delta\lambda)$ is the so-called lineshape function which describes how sensitive each channel is to a wavelength $\Delta\lambda$ away from its center wavelength. The lineshape function is typically in the shape of a peak centered at $\Delta\lambda = 0$ and should be normalized so that $\int f(\Delta\lambda) d\Delta\lambda = 1$. Combining (3.6) and (3.7) gives:

$$I_j = \int a(\lambda) f(\lambda - \lambda_j) I(\lambda) d\lambda. \quad (3.8)$$

Here we can see that the instrument transform is a type of convolution of the true spectrum with the instrument lineshape onto a discrete grid. The width of the lineshape function peak is the resolution of the spectrometer, as it determines the smallest wavelength scale at which spectral features can be distinguished. The spacing between the center wavelengths λ_j is often referred to as the sampling resolution. The ratio between the sampling resolution and the resolution is called the sampling ratio.

Now that we have a model for how the spectral measurements work, we can apply that to the absorption equation we want to solve. If we combine (3.3) and (3.8) we get:

$$\begin{aligned} I_j &= \int a(\lambda) f(\lambda - \lambda_j) I(\lambda) d\lambda \\ &= \int a(\lambda) f(\lambda - \lambda_j) I_0(\lambda) \exp\left(-\sum_i S_i \sigma_i(\lambda)\right) d\lambda. \end{aligned} \quad (3.9)$$

To be able to simplify the right hand side of (3.9) we must make a few assumptions. If we assume that the sum in the exponential is small enough that the linear approximation $\exp(x) \approx 1 + x$ is valid we can write:

$$\begin{aligned}
I_j &\approx \int a(\lambda) f(\lambda - \lambda_j) I_0(\lambda) \left(1 - \sum_i S_i \sigma_i(\lambda) \right) d\lambda \\
&= I_{0,j} - \sum_i S_i \int a(\lambda) f(\lambda - \lambda_j) I_0(\lambda) \sigma_i(\lambda) d\lambda,
\end{aligned} \tag{3.10}$$

where $I_{0,j}$ is the instrument transform of $I_0(\lambda)$. To further simplify (3.10) we conjecture that the following approximation is valid:

$$\begin{aligned}
&\int a(\lambda) f(\lambda - \lambda_j) I_0(\lambda) \sigma_i(\lambda) d\lambda \\
&\approx \int a(\lambda) f(\lambda - \lambda_j) I_0(\lambda) d\lambda \int f(\lambda - \lambda_j) \sigma_i(\lambda) d\lambda = I_{0,j} \sigma_{i,j},
\end{aligned} \tag{3.11}$$

where $\sigma_{i,j}$ is the absorption cross section $\sigma_i(\lambda)$ convoluted with the lineshape function. Using (3.11) in (3.10) gives us:

$$I_j \approx I_{0,j} \left(1 - \sum_i S_i \sigma_{i,j} \right) \approx I_{0,j} \exp \left(- \sum_i S_i \sigma_{i,j} \right). \tag{3.12}$$

Now we have arrived at a version of (3.3), but for spectra measured with a spectrometer. This can in turn be rewritten as an equivalent to (3.4):

$$- \log \left(\frac{I_j}{I_{0,j}} \right) \approx \sum_i S_i \sigma_{i,j}. \tag{3.13}$$

This is effectively the equation that is solved in many standard absorption spectroscopy applications. Although it looks very similar to (3.4), which has a more general validity, it is important to remember the assumptions that were used to derive it. Firstly, the linear approximation of the exponential was assumed to be valid, which depends on the true optical density being small ($\ll 1$) for all wavelengths. If this applies the absorbers are said to be optically thin. Secondly, the approximation in (3.11) was assumed to be valid. Although no proof will be given here, this assumption will typically hold given that at least one of $I_0(\lambda)$ and $\sigma_i(\lambda)$ does not exhibit large variations on the scale of the width of the lineshape function (i.e. the instrument resolution). However, the assumption may still hold approximately when both $I_0(\lambda)$ and $\sigma_i(\lambda)$ have large variations on the scale of the instrument resolution, if these variations are sufficiently uncorrelated. Both of these assumption are valid in many applications, but for the cases when they are not, slightly different approaches need to be used.

3.1.2 Spectral fitting algorithms

Finding the set of column densities that best match the measured spectra is called spectral fitting or spectral retrieval. This is typically done by some form of multivariate optimization. The simplest form of this is linear least squares fitting. Equation (3.13), which was derived in the previous section, is a linear equation system in the unknown column densities S_i , and could thereby be solved by linear least squares. However, to arrive at this equation it was assumed that molecular absorption was the only effect changing the intensity of the light. In most cases light scattering out of the light path, either from Rayleigh scattering or aerosol scattering, needs to be considered too. Fortunately, light losses due to scattering also obey the Beer–Lambert law, but its cross sections generally has a fairly smooth wavelength dependence. For this reason it can, within a limited wavelength range, be accounted for by a low order polynomial whose coefficients must also be determined by the spectral fitting. With this polynomial included, the equation system to be solved becomes:

$$-\log\left(\frac{I_j}{I_{0,j}}\right) = \sum_i S_i \sigma_{i,j} + \sum_{i=0}^n c_i \lambda_j^i, \quad (3.14)$$

where c_i are the unknown coefficients of the polynomial. This is still a linear equation system, but in the variables S_i and c_i . This equation system may also be written in matrix form:

$$\mathbf{y} = A\mathbf{x}, \quad (3.15)$$

where \mathbf{y} is the vector of the optical densities for the measured channels, A is a matrix with the convoluted cross sections $\sigma_{i,j}$ and polynomial components λ_j^i as columns, and \mathbf{x} is a vector of the unknown variables S_i and c_i . Assuming the number of unknown variables, i.e. the number of molecular absorbers considered plus the number of polynomial components, is smaller than the number of wavelength channels considered, this equation system is overdetermined and can be solved by least squares. The least squares solution to this equation can be expressed in terms of the pseudoinverse of A , A^+ :

$$\mathbf{x} = A^+ \mathbf{y} \quad (3.16)$$

$$A^+ = (A^T A)^{-1} A^T. \quad (3.17)$$

The pseudoinverse is used here for conceptual clarity. In practice, other methods to find the least squares solution, such as QR decomposition of A , are used since they are more computationally efficient and numerically stable.

Although a simple linear least squares fitting routine is good enough in some applications, it is often necessary to account for additional effects that may break the linear relationship. Common examples of this are strong non-linear absorption effects and instrumental effects such as wavelength shifts or stray light. In the most general case, a non-linear spectral fitting routine may need to solve an equation system of the form:

$$\mathbf{y} = \mathbf{f}(\mathbf{x}), \quad (3.18)$$

where $\mathbf{f}(\mathbf{x})$ is a set of non-linear functions. A least squares solution to this non-linear equation may be found with an iterative method, such as the Gauss–Newton algorithm. Starting from an initial guess x_0 , the next iteration is calculated as:

$$\mathbf{x}_{k+1} = \mathbf{x}_k + J^+(\mathbf{x}_k)(\mathbf{y} - \mathbf{f}(\mathbf{x}_k)), \quad (3.19)$$

where $J(\mathbf{x})$ is the Jacobian of $\mathbf{f}(\mathbf{x})$, i.e. $J_{i,j} = \partial f_i(\mathbf{x}) / \partial x_j$ and J^+ is the pseudoinverse of J . Although the Gauss–Newton algorithm converges very fast when close to the least squares solution, it can be unstable when further away from it. For this reason, a modified version of the Gauss–Newton algorithm, the Levenberg–Marquardt algorithm, is typically used instead.

Compared to the linear least squares method, iterative non-linear least squares methods can be significantly slower and are not guaranteed not find the global least squares solution. These disadvantages are often amplified as the number of degrees of freedom, i.e. the number of elements in \mathbf{x} grows. For this reason, it is often beneficial to use a hybrid of linear and non-linear least squares, where as many parameters as possible are treated linearly. One form of equation that can often be relevant to solve is:

$$\mathbf{y}(\mathbf{p}) = A\mathbf{x}. \quad (3.20)$$

This is typically a version of equation (3.15) where the left hand side still represent the optical density of the measured spectrum and the right hand side is a linear combination of absorption cross sections, but where the optical density has a non-linear dependency on a number of parameters \mathbf{p} . This dependency may for instance represent a number of corrections for instrumental changes between the reference spectrum and the evaluated spectrum, such as wavelength shifts and stray light. This equation needs to be optimized with respect to both \mathbf{x} and \mathbf{p} . For a given value of \mathbf{p} the linear least squares solution for \mathbf{x} is given by:

$$\mathbf{x} = A^+ \mathbf{y}(\mathbf{p}). \quad (3.21)$$

If we insert this solution into (3.20) the equation to be solved can be written:

$$0 = \mathbf{y}(\mathbf{p}) - AA^+ \mathbf{y}(\mathbf{p}) = (I - AA^+) \mathbf{y}(\mathbf{p}), \quad (3.22)$$

where I is the identity matrix. If solving this equation for \mathbf{p} using the Gauss–Newton algorithm, the iterative function would be:

$$\mathbf{p}_{k+1} = \mathbf{p}_k - [(I - AA^+)J_y(\mathbf{p}_k)]^+ (I - AA^+) \mathbf{y}(\mathbf{p}_k), \quad (3.23)$$

where $J_p(\mathbf{p})$ is the Jacobian of $\mathbf{y}(\mathbf{p})$. Once a solution for \mathbf{p} is obtained, the solution for \mathbf{x} can be obtained using (3.21). As in the more general non-linear case discussed above, the Gauss–Newton solution is presented here because of its relative simplicity. In real applications the Levenberg–Marquardt algorithm is typically preferred due to its stability far from the least squares solution. This hybrid method is for example implemented in the DOAS spectral evaluation software QDOAS [11] which has been used for all of the DOAS evaluations in this thesis.

3.2 Flux measurements

The result from a spectral fitting routine, as described above, is typically in the form of columns or differential columns. As defined in equation (3.2) a column is the path integral of the number density of a species along a light path. If the number density is constant along the path, the column is the number density multiplied by the path distance. In many spectroscopic applications, the quantity of interest is number density. For example, the concentrations of a number of species might be tracked in a laboratory reactor cell by making spectroscopic measurements along a fixed path in it. The spectroscopic retrieval of the measured spectra gives columns and number densities are obtained by dividing the column by the fixed path length. If the concentration is not homogeneous in the cell, this will give an average of the number densities along the light path.

For the purpose of measurements of gas fluxes, however, there is a great advantage to measuring columns instead of just number densities. The mass flux \dot{m}_i of species i through a surface B in the atmosphere can be written as a surface integral:

$$\dot{m}_i = \iint_B \rho_i(\mathbf{v} \cdot \mathbf{n}) dA, \quad (3.24)$$

where ρ_i is the mass density of the species, \mathbf{v} is the wind velocity vector and \mathbf{n} is the normalized vector normal to the surface. The mass density is of course proportional to the number density n_i of the same species: $\rho_i = M_i n_i / N_a$ where M_i is the molar mass of the species and N_a is the Avogadro constant. If you want

to calculate the surface integral of a quantity, it is a great convenience to be able to directly measure the integral of that quantity along one dimension. In SOF and Mobile DOAS, the two flux measurement methods discussed in this thesis, spectroscopic measurements are made using an instrument in a measurement vehicle along an open light path from the instrument to the sky. As the vehicle moves on the ground, the light path slices through the atmosphere, forming a surface. Assuming that the direction of the light path remains constant as the vehicle moves, the surface integral in equation (3.24), with this surface as B , can be written:

$$\dot{m}_i = \int_V \left[\int_P \rho_i dl \right] \mathbf{v} \cdot (\hat{\mathbf{z}} \times d\mathbf{x}), \quad (3.25)$$

where P is the measurement light path, V is the path driven by the vehicle and $\hat{\mathbf{z}}$ is a normalized vector in the direction of the measurement path. Using the proportionality of mass and number density and the definition in equation (3.2), the inner integral can be written:

$$\int_P \rho_i dl = \int_P \frac{M_i}{N_a} n_i dl = \frac{M_i}{N_a} S_i, \quad (3.26)$$

which allows equation (3.25) to be written:

$$\dot{m}_i = \frac{M_i}{N_a} \int_V S_i \mathbf{v} \cdot (\hat{\mathbf{z}} \times d\mathbf{x}). \quad (3.27)$$

Since S_i is given by the spectral retrieval for the species possible to measure with the instrument, only the outer integral along the ground path needs to be addressed. Since each spectral measurement takes a finite amount of time, the spectral retrieval will give a discrete series of S_i :s for each species. Hence, the integral has to be approximated by a sum. Since horizontal movement typically dominates for a ground vehicle, $d\mathbf{x}$ can be assumed to be in the horizontal plane. For this reason, only the angle between the light path and zenith matters for the cross product with $\hat{\mathbf{z}}$. Furthermore, since the horizontal wind component typically dominates over the vertical component, and since $\hat{\mathbf{z}}$ is fairly close to vertical in most measurements, the vertical wind component can typically be neglected. Using these assumptions, equation (3.27) can be approximated by:

$$\dot{m}_i = \frac{M_i}{N_a} \sum_j S_{ij} v_j \cos(\theta_j) \sin(\alpha_j) d_j, \quad (3.28)$$

where S_{ij} is the column of species i retrieved from spectrum j in a measurement series, v_j is the wind speed at that time, θ_j is the angle of the light path from zenith, α_j is the angle between the wind direction and driving direction, and d_j

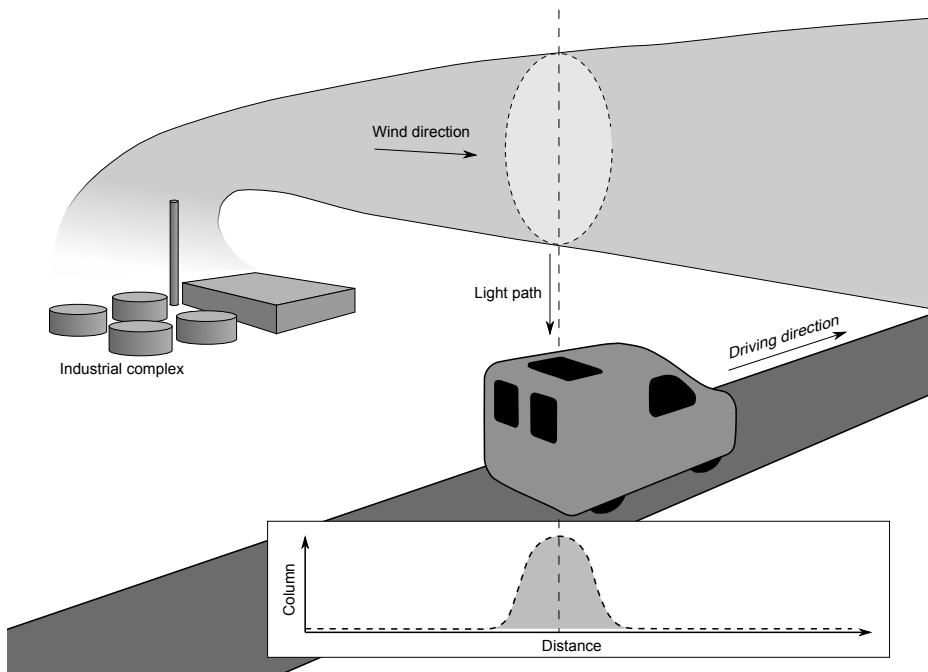


Figure 3.1: Illustration of the principles of flux measurements in an industrial plume. The plume appears as a peak in the series of measured columns on top of an ideally constant background. The area under the peak, multiplied by the wind speed and geometric corrections, corresponds to the flux in the plume of the species measured.

is the distance traveled during the measurement of the spectrum. This is the formula that is typically used for flux calculations in SOF and Mobile DOAS. In addition to the spectral measurements, the position of the vehicle needs to be logged carefully with a GPS-receiver to calculate d_j and the driving direction, and some form of wind data is needed. Wind measurements are discussed in section 3.5.

Equation (3.28) in theory applies to any column measurements from a vehicle along any conceivable measurement path driven. For the purpose of measuring emission fluxes from local sources, certain specific measurement strategies are typically used. First of all, the spectroscopic retrieval is typically made relative to a reference spectrum measured in a location assumed to be free from local emissions. The evaluated columns from such a retrieval are not absolute, but relative to the background column present in the reference spectrum. This is called a differential measurement. This is partly motivated because differential spectral evaluations are typically easier to make and more precise. But the differential column is also the relevant quantity for calculating the flux from a local

source. Figure 3.1 illustrates how a typical flux measurement is made nearby a local industrial facility. The differential column is measured continuously while driving along a road downwind of the industry. Before and after intercepting the plume, the evaluated column remains fairly constant around zero. As the path of the measured light cuts through the plume, the evaluated column of the species measured rises to a peak value and then goes back down to zero. The area under the peak multiplied by the wind speed and geometrical corrections gives the flux in the plume. If there are variations in the background concentration, the evaluated column might not stay constant at zero before and after the plume. In such cases it is important to determine a baseline that matches the column right before and after passing the plume and to include only the area above that baseline. If the background concentration varies too much or over too short distances, it will be difficult to separate the plume from the background variations, increasing the uncertainty of the flux measurement or even making it useless.

Downwind measurements are typically combined with similar upwind measurements. If there are no significant emission sources close-by on the upwind side, only one or a couple of measurements is typically needed to verify this. If significant upwind sources exist, the incoming flux from these sources needs to be measured regularly to be subtracted from the flux downwind of the source of interest. If the upwind sources are large compared to the downwind source, the accuracy will be worse for this difference between the two fluxes. If possible, the measurements of emissions from an industrial facility might be chosen to be made in a wind direction for which there are no upwind sources in order to decrease this uncertainty.

The measurement route should ideally be as perpendicular to the wind direction as possible. Due to the $\sin(\alpha_j)$ factor in equation (3.28), the flux calculation has the highest sensitivity to uncertainty in wind direction when α_j is close to 90° .

As an emission plume travels further downwind from its source it spreads out, both in the horizontal direction and in the vertical direction. For wind measurement uncertainty reasons it is typically best to let the plume mix as high up as possible before measuring the flux. However, as the plume is dispersed in the horizontal direction, the size of columns will decrease, which increases the uncertainty due to background variations. The optimal downwind distance to measure is therefore a trade-off between these two effects and depends on the magnitude of the flux, the wind speed, how fast the plume is dispersed etc. In practice the choice of downwind distance is often severely limited by the existence of suitable measurement roads. Typical downwind distances for flux measurements of emissions from industries range from a few hundred meters to several kilometers. The optimal driving speed for flux measurements depends on a similar trade-off. Driving too slow increases uncertainties due to changes in wind and background concentrations that occur during the transect. Driving too fast while measuring a narrow plume will give a sparsely sampled plume, sometimes with only a

couple of measurement points, also increasing the uncertainty. The quality of the road also affects how fast the measurement vehicle can be driven without vibrations affecting the spectroscopic measurements negatively. Measurement speeds between 30 and 70 km/h are typically used, but both slower and faster measurements are sometimes made.

3.3 Solar Occultation Flux

Solar Occultation Flux (SOF) is a flux measurement method based on spectroscopy of direct sun light in the mid-infrared wavelength region, approximately 2–20 μm (500–5000 cm^{-1}), from a mobile platform. The mid-infrared wavelength region is used for molecular spectroscopy in many different applications since most molecular species have some form of absorption in this region. All of these are, however, not suitable for SOF measurements. Some species cannot be measured because they absorb in wavelength bands that are almost depleted of sun light at ground level due to absorption by atmospheric background species, mainly water (H_2O) and carbon dioxide (CO_2). Other species have absorption cross sections that are too weak, giving a detection limit that is too large to be practically useful. A few species, mainly methane (CH_4), nitrous oxide (N_2O), water and carbon dioxide, are difficult to measure because the atmospheric background columns of the species themselves are so high. Measuring them may be likened to observing the flame of a candle in front of the sun. SOF measurements of industrial emissions have been made on a regular basis by the Optical remote sensing group since 2002, but the first peer-reviewed publication was Paper I. Similar measurements of volcanic emissions have also been made by [12, 13].

Since atmospheric scattering is much weaker in the mid-infrared region than in the visible and ultraviolet regions (Rayleigh scattering is proportional to λ^{-4}), there is very little mid-infrared light when performing sky measurements in any other direction than towards the sun. For the longer wavelengths in this region $> 5 \mu\text{m}$, thermal radiation from the atmosphere itself becomes significant, but this cannot be used for absorption spectroscopy since there is too little temperature contrast between the gases of interest and the background atmosphere. This leaves direct sun light as the only practically useful natural light source for absorption spectroscopy in this region. The solar disk, however, only covers about 0.5° of the sky and it moves by approximately $0.25^\circ/\text{minute}$, so for spectroscopic measurements of direct sun light this motion must be tracked very carefully.

Since direct-sun measurements are dependent on clear weather, it is not possible to measure at all times and some times it may be necessary to wait several days for suitable conditions to perform measurements. On the other hand, clear weather is also associated with convective instability which is beneficial for all flux measurements because it increases vertical mixing of emission plumes and smooths out vertical gradients in wind speeds. Direct sun measurements also have the advantage that there is very little uncertainty in the average light path

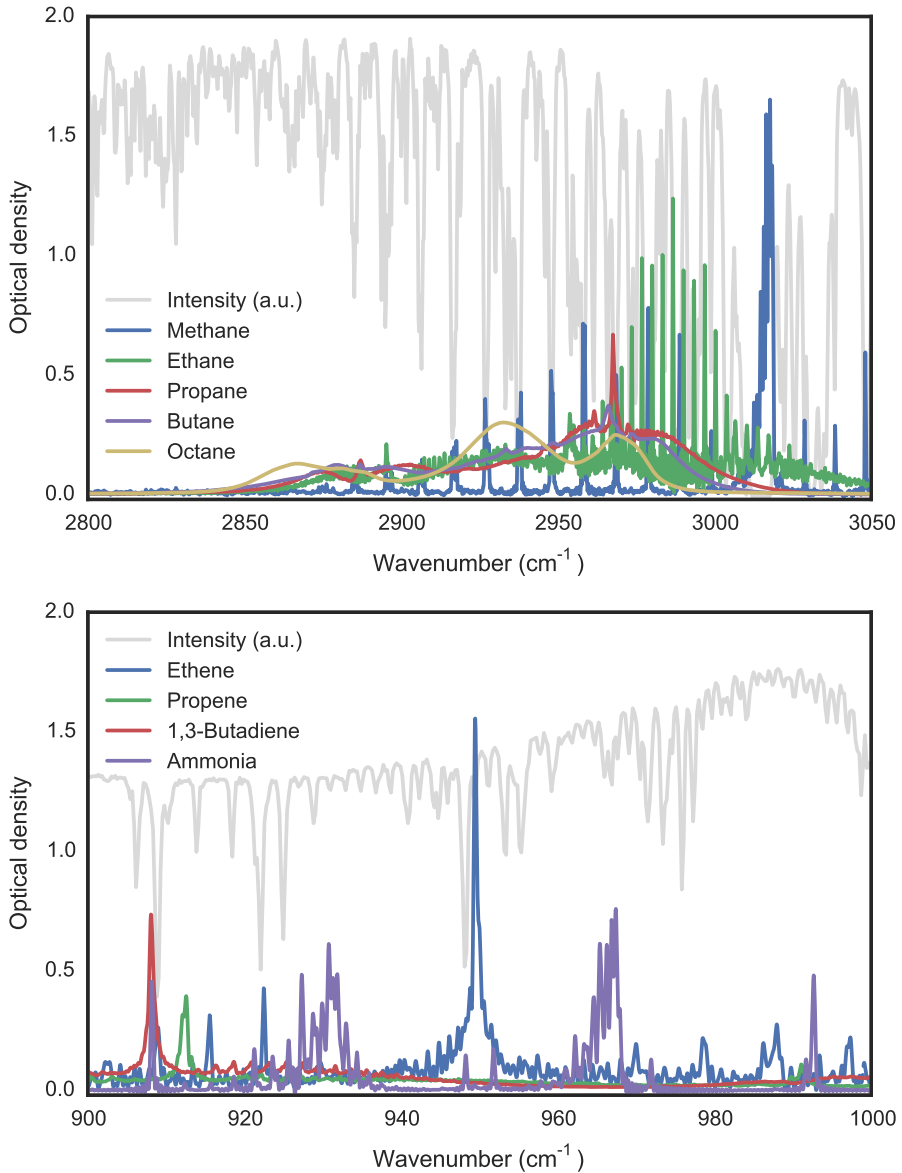


Figure 3.2: Absorption cross sections for some of the molecular species that can be measured in the C–H stretch region (upper panel) and in the fingerprint region (lower panel). The optical density spectrum of a mass column of 1 g/m^2 of each species is downgraded to 0.5 cm^{-1} resolution and shown together with typical solar spectra of the same resolution (grey lines).

of the measured light. All the measured light can be assumed to have passed the plume in the sun light direction, which means θ_j in (3.28) should be the solar zenith angle (SZA) at the time of the measurement. This angle can be calculated with high accuracy based on the latitude, longitude, date and time of the measurement [14]. Another example of infrared direct sun spectroscopy are the stationary high resolution solar measurements made within NDACC (Network for the Detection of Atmospheric Composition Change), a network of observatories to monitor long-term trends in atmospheric composition [15]. These typically employ a passive solar tracker that calculates the position of the sun based on their position, date and time of day and direct the field of view of the spectrometer with a set of mirrors in a mechanical device. Some of them also has an active step, which fine-tunes the measurement direction so that the light enters the spectrometer in the exact same direction at all times.

Each molecular species is typically associated with a number of infrared absorption bands, each corresponding to excitation of a specific vibrational mode of that molecule. The fine structure within that band is a result of excitations from different ground states and simultaneous excitation of rotational modes. Molecules of similar composition and structure tend to have absorption bands close to each other, often with partial overlap. For instance molecules with C–H bonds typically have an absorption band in the region $2800\text{--}3000\text{ cm}^{-1}$ associated with a stretching vibrational mode. This region is known as the C–H stretch region and is of particular interest to SOF for the possibility of measuring a broad range of hydrocarbons and other VOCs. Another wavelength region of particular interest for SOF measurements is the so called fingerprint region, approximately $500\text{--}1500\text{ cm}^{-1}$, which is associated with bending vibrational modes. It is called the fingerprint region because many molecules have fairly unique absorption signatures in it, enabling more detailed speciation compared to the C–H stretch region. Although many molecules have unique absorption signatures in the fingerprint region, few of them are strong enough to achieve a useful detection limit for SOF measurements. Alkenes, in particular small alkenes, is one class of molecules that tend to have strong absorption cross sections in the fingerprint region.

A few examples of absorption cross sections of species absorbing in the C–H stretch and fingerprint regions are shown in figure 3.2. In the C–H stretch region the cross sections of a number of alkanes are shown, illustrating that they all have overlapping absorption signatures with the smaller molecules (methane and ethane) featuring narrower absorption lines and the larger molecules having smoother absorption features shifted towards lower wavenumbers. A typical solar spectrum in the same region shows that significantly less light is available above 3000 cm^{-1} . This is mainly due to absorption from water and methane. Since methane is much more abundant in the atmosphere than the other VOCs, the solar spectrum is nearly depleted of light in its narrow absorption lines. This makes it particularly difficult to measure methane by solar spectroscopy compared to the other VOCs. The cross sections of a number of alkenes and

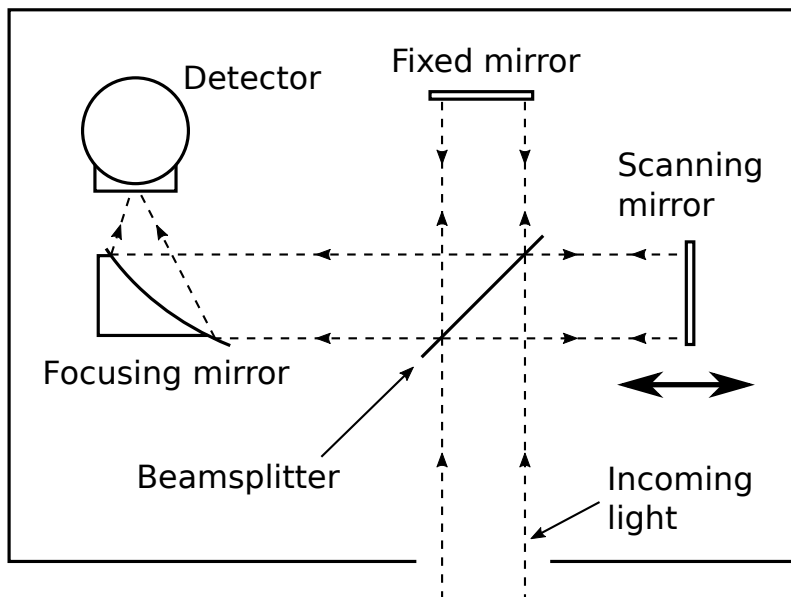


Figure 3.3: Simplified drawing illustrating the principles of an FTIR spectrometer based on a Michelson interferometer. Light enters the spectrometer and is split into two paths by a beamsplitter. The two beams are reflected by two mirrors and recombined at the beamsplitter. The recombined light is focused on an infrared detector. The path difference between the two beams is varied by scanning one of the mirrors back and forth.

ammonia in the fingerprint region is shown in the lower panel of figure 3.2. Here it can be seen that the absorption cross sections are less overlapping, often consisting of one strong narrow absorption line and a number of weaker ones with some distance in between.

3.3.1 Instruments

FTIR spectrometer

Spectra in the mid-infrared region are generally measured with FTIR (Fourier Transform InfraRed) spectrometers, since they offer better signal-to-noise ratios than scanning monochromators due to Fellgett's advantage [16]. The basic principle of an FTIR spectrometer is illustrated in figure 3.3. The spectrometer consists of a Michelson interferometer [17] with a moving mirror at one of the arms and an infrared detector which the recombined light is focused onto. The detector records the intensity of the recombined light as the path difference is varied by the moving mirror. In real FTIR spectrometers the layout of the optics is often not the same as in 3.3 but the principle is the same. If the light intensity

of the incoming light as a function of wavenumber $\bar{\nu}$ (wavenumber is the inverse of wavelength $\bar{\nu} = 1/\lambda$) is denoted $I(\bar{\nu})$, the intensity recorded by the detector as a function of path difference δ , called an interferogram, is given by [18]:

$$J(\delta) = \int_{-\infty}^{\infty} I(\bar{\nu}) \cos(2\pi\bar{\nu}\delta) d\bar{\nu}. \quad (3.29)$$

Equation (3.29) describes a cosine Fourier transform and if $J(\delta)$ could be obtained for all values of δ , this transform could be inverted to get a full resolution spectrum:

$$I(\bar{\nu}) = \int_{-\infty}^{\infty} J(\delta) \cos(2\pi\bar{\nu}\delta) d\delta. \quad (3.30)$$

In a physical instrument there is of course a limit to how large δ the interferogram can be recorded for. If the interferogram is only recorded in the interval $-L$ to L , a degraded spectrum $I_D(\bar{\nu})$ can be calculated as a truncated cosine Fourier transform:

$$I_D(\bar{\nu}) = \int_{-L}^L J(\delta) \cos(2\pi\bar{\nu}\delta) d\delta = \int_{-L}^L J(\delta) D(\delta) \cos(2\pi\bar{\nu}\delta) d\delta, \quad (3.31)$$

where $D(\delta)$ is a boxcar function: $D(\delta) = 1$ for $|\delta| \leq L$, $D(\delta) = 0$ for $|\delta| > L$. The right hand side of (3.29) is a cosine Fourier transform of a product of two functions which is the same as the convolution of the cosine Fourier transforms of each function. This means that the result is the convolution of the real spectrum with the cosine Fourier transform of the boxcar function $D(\delta)$ which can be proven to be:

$$f(\bar{\nu}) = \int_{-\infty}^{\infty} D(\delta) \cos(2\pi\bar{\nu}\delta) d\delta = 2L \frac{\sin(2\pi\bar{\nu}L)}{2\pi\bar{\nu}L} = 2L \operatorname{sinc}(2\pi\bar{\nu}L). \quad (3.32)$$

Hence we can think of $f(\bar{\nu})$ as the effective lineshape function when measuring the spectrum $I_D(\bar{\nu})$. This lineshape function has a full width at half maximum of approximately $0.605/L$ but it also has an infinite series of side lobes decreasing in amplitude with distance from the center. The side lobes can be suppressed by using another function, called apodization function, for $D(\delta)$ in (3.31) which transitions more continuously to 0 at $|\delta| > L$, but this comes at the expense of increasing the width of the lineshape function. Many different choices of apodization function can be used to calculate a spectrum from the measured

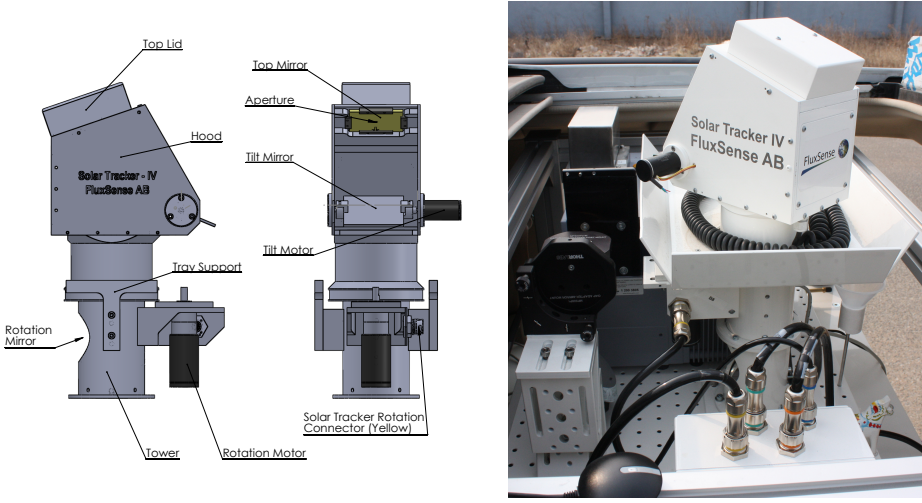


Figure 3.4: Illustration drawing of a solar tracker used for SOF measurements (left) and a photograph of a similar solar tracker mounted together with an FTIR spectrometer and transfer optics as a complete SOF system inside a measurement vehicle (right).

interferogram and the choice determines which lineshape function $f(\bar{\nu})$ should be used to degrade the cross sections in the spectral retrieval routine. For most of the work in this thesis, an apodization function called Norton–Beer weak [19] has been used.

A real interferogram can of course only be sampled in a finite number of values of δ . Hence the integral in (3.31) is generally calculated as a sum over a number of equally distant samples of the interferogram $J(\delta)$. The number of sampling points required, N_s , to measure a spectrum in the range $\bar{\nu}_{\min}$ to $\bar{\nu}_{\max}$ with resolution, $\Delta\bar{\nu}$, is given by [18]:

$$N_s = \frac{2(\bar{\nu}_{\max} - \bar{\nu}_{\min})}{\Delta\bar{\nu}}. \quad (3.33)$$

To ensure equally distant samples of the interferogram, a laser beam is typically sent through the interferometer in parallel with the measured light and detected by a separate detector. The sampling of the interferogram is then triggered by the maxima and the minima of the laser beam intensity. This also enables an absolute and very exact wavelength calibration of the resulting spectra.

Solar tracker

For stationary direct-sun measurements, such as the measurements made within the NDACC network, the solar tracker only needs to keep track of the sun's apparent movement across the sky due to earth's rotation, which is a continuous but relatively slow movement. For mobile direct-sun measurements, the solar

tracker also needs to compensate for the movements of the measurement vehicle, including turning, tilting, shocks and vibrations. Since these movements can cause much faster angular displacements of the instrument relative to the sun than that caused by the sun's movement across the sky, the solar tracker used for SOF measurements generally needs to be faster than one used for stationary measurements. The irregular and unpredictable nature of the movement of a measurement vehicle also makes it less practical to apply the passive solar tracking approach which is often used for stationary measurements, i.e. calculating the position of the sun relative to the instrument and using that to guide the solar tracker. Passive solar tracking could in principle be possible for a mobile system if the orientation of the instrument could be tracked very fast and accurately, but so far all solar trackers used for SOF measurements have been based on active solar tracking, i.e. the viewing direction of the instrument is guided by a closed control loop regulating the angle of the incoming light as measured by some form of sensor.

Figure 3.4 shows an example of a solar tracker that was originally developed for SOF measurements by the Optical remote sensing group [20] at Chalmers University of Technology. In this solar tracker the light is guided by two mirrors mounted on a rotating head. The first mirror, called the tilt mirror, is mounted on an electric motor, allowing it be tilted back and forth. By controlling the rotation of the head and the tilt of the tilt mirror, the incoming sun light can be made to reflect on the tilt mirror up to the top mirror and down through the rotational axis of the tracker, regardless of the sun's relative position. In the top mirror there is a small aperture diverting a fraction of the incoming light into a small box, where it is projected onto an optical position sensor. By controlling the rotation and tilt motors, a feedback loop maintains the position of the diverted light on the optical position sensor at an adjustable setpoint. If the setpoint is chosen correctly this will mean that the light always comes out at the same angle through the exit hole at the bottom of the solar tracker tower. From there it is guided into the FTIR spectrometer by means of an optical setup that enables some further adjustments.

3.3.2 Spectral retrievals

The spectral retrieval routines for the SOF measurements in this thesis have been implemented in the spectral retrieval software QESOF [20]. This software implements a hybrid fitting algorithm which makes a linear fit as a first guess and uses this as a starting point for a second non-linear fit. The non-linear algorithm enables fitting of strong non-linear absorption and wavelength shifts. Most SOF measurements performed so far have been made in either an alkane mode or an alkene mode. The alkane mode is based on the broadband absorption of a wide range of VOCs in the C–H stretch region, $2800\text{--}3000\text{ cm}^{-1}$, as illustrated in figure 3.2. This measurement mode is presented and discussed in Paper III. Even though it is called alkane mode, the retrieval is sensitive to a wide range of VOCs, not just alkanes. Alkanes, however, tend to have the strongest absorption per

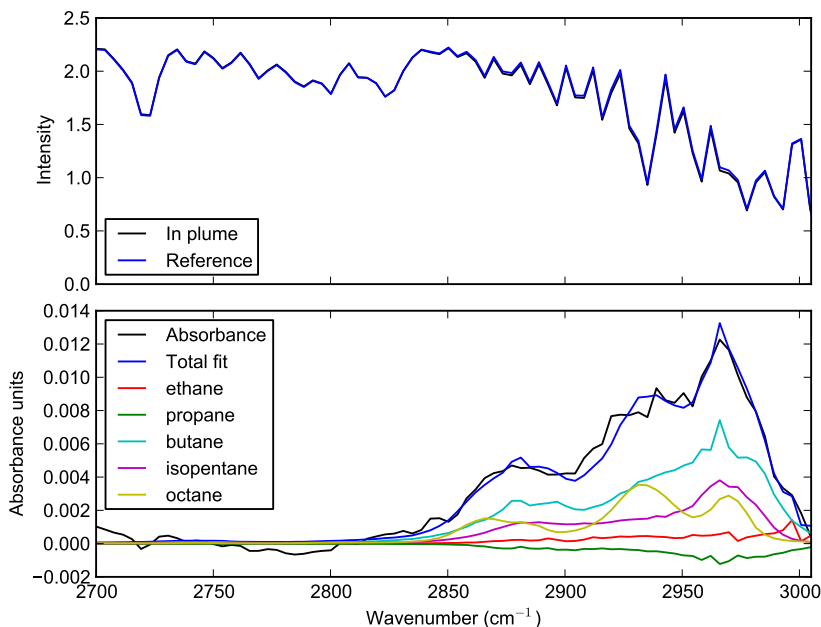


Figure 3.5: A solar spectrum measured in an emission plume and a reference spectrum (top panel), the actual and fitted alkane absorption and the fitted components of ethane, propane, butane, isopentane and octane (lower panel).

mass in this region and industrial VOC emissions, especially refinery emissions, are generally dominated by alkanes. Since the absorption of VOCs in this region is so broadbanded, high resolution measurements are not necessary. Instead an 8 cm^{-1} resolution is typically used.

The spectral retrieval routine for this mode uses a $2725\text{--}3005 \text{ cm}^{-1}$ fitting window and includes cross sections of ethane (C_2H_6), propane (C_3H_8), n-butane (C_4H_{10}), isopentane (C_5H_{12}) and n-octane (C_8H_{18}). Although the actual absorbing VOC mixture measured may not be composed specifically of these species, they generally do a good job fitting the absorbance and approximating the total mass column of VOCs, since the absorption signatures are similar and the total absorption is roughly proportional to the molecule mass for most alkanes. The specific alkanes included were chosen because they are common species and because they together represent much of the variability among the absorption cross sections of the different alkanes. Although methane also has strong absorption in this region, the measurements are not very sensitive to this because methane's narrow absorption lines are nearly depleted of light due to the large background column in the atmosphere. In Paper III it was shown that the spectral retrieval

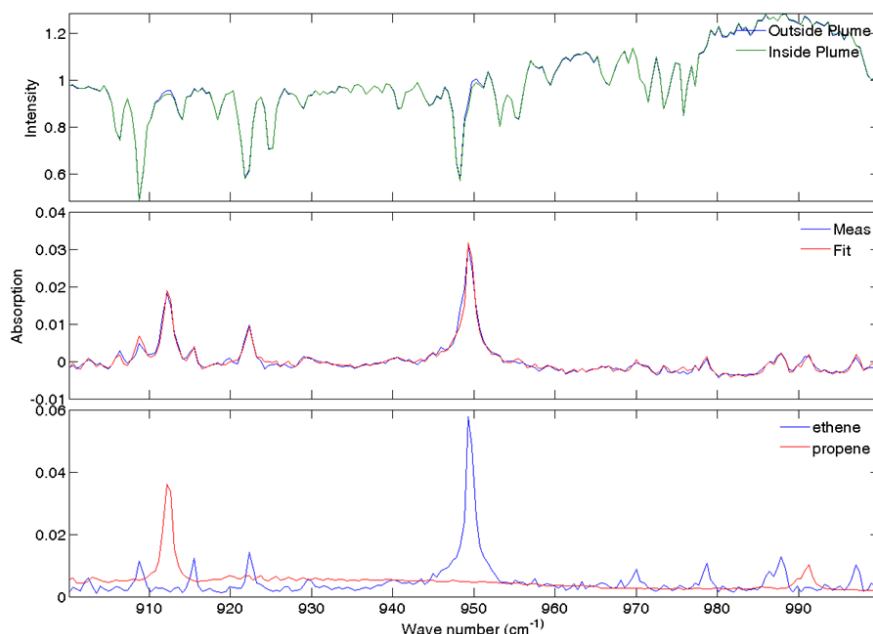


Figure 3.6: The top plot shows a spectrum measured in a plume as well as a reference spectrum measured outside the plume. The middle plot shows the differential absorbance between the two spectra and the fit of the alkene spectral retrieval routine. The lower plot shows the absorption cross sections of ethene and propene.

correctly determined the total non-methane VOC mass columns within 7% for synthesized absorption spectra with actual VOC compositions measured in situ downwind of refineries during 7 separate episodes. Figure 3.6 shows an example of a linear combination of the alkane cross sections fit to a measured absorbance. Additional cross sections for water, heavy water (HDO), methane, and a second order polynomial are also included in the retrieval to improve the spectral fit and avoid interference. The retrieved methane column is not included in the resulting total alkane mass column because it is highly uncertain and typically not of interest.

The alkene mode SOF measurements are based on the more narrow absorption peaks of alkenes, primarily ethene (C_2H_4) and propene (C_3H_6) (also known as ethylene and propylene), in the fingerprint region, $500\text{--}1500\text{ cm}^{-1}$, as exemplified in figure 3.2. This measurement mode is described in detail in Paper I. Ethene and propene both have strong narrow absorption peaks in the fingerprint region, especially ethene, and they are commonly used in large quantities in petrochemical industries, especially as feedstock for polyethylene and polypropylene plants. The spectral retrieval routine for this mode uses a $900\text{--}1000\text{ cm}^{-1}$ and includes cross sections for ethene, propene, water, carbon dioxide, ammonia (NH_3), ozone

(O₃) and a 4th order polynomial. This spectral retrieval has also been used to measure ammonia several times and in a few instances more exotic species such as 1,3-butadiene and isobutene [21] in situations with large emissions of those species (this of course requires cross sections of those species to be included in the retrieval). Figure 3.6 shows an example of a spectral fit of the absorbance of ethene and propene for the alkene mode. In the fingerprint region thermal radiation from the atmosphere and the instrument itself becomes significant. For this reason it is important to regularly measure so called dark spectra, i.e. spectra with the instrument viewing the clear sky, and use these to subtract the thermal radiation intensity from the solar spectra.

3.4 Mobile DOAS

Differential Optical Absorption Spectroscopy (DOAS) is a spectroscopic method used for measurements in the visible and ultraviolet wavelength regions. In this region molecular absorption is generally caused by excitations of valence electrons in the molecules. DOAS was originally developed by Perner and Platt [22–24] and has been used in a wide array of applications. A key difference between DOAS and infrared spectroscopy is the strong presence of scattering at these wavelengths. Rayleigh scattering by molecules is proportional to λ^{-4} and hence increases strongly with decreasing wavelength.

3.4.1 Instruments

Because spectral measurements in the visible and ultraviolet regions are often limited by statistical photon noise (or shot noise) and because array detectors are cheaply available, FTIR spectrometers do not have the same advantage as they have in the infrared region. The most common instrument used for DOAS applications is instead a Czerny–Turner spectrometer with an array detector. The basic principle of an Czerny–Turner spectrometer is illustrated in figure 3.7. The light enters the spectrometer through a slit and is reflected by a collimating mirror onto a reflective diffraction grating. The grating causes wavelength dispersion in the collimated light which is then focused onto the array detector. Due to the wavelength dispersion, the position of the focal point on the array detector is shifted with wavelength. For the diffraction grating, the reflection angle of maximum intensity α_m is related to the incidence angle α_i through the formula:

$$d(\sin \alpha_i + \sin \alpha_m) = n\lambda, \quad (3.34)$$

where d is the inter-slit distance of the grating, n is the diffraction order, and λ is the wavelength. Usually the first diffraction order is used so $n = 1$. From (3.34) it follows that a smaller d gives a larger wavelength dispersion. Hence the width of the wavelength range of a spectrometer is normally controlled by selection of a grating with suitable d . The wavelength range measured can similarly be shifted by rotating the grating. The instrument line shape function is the result of a

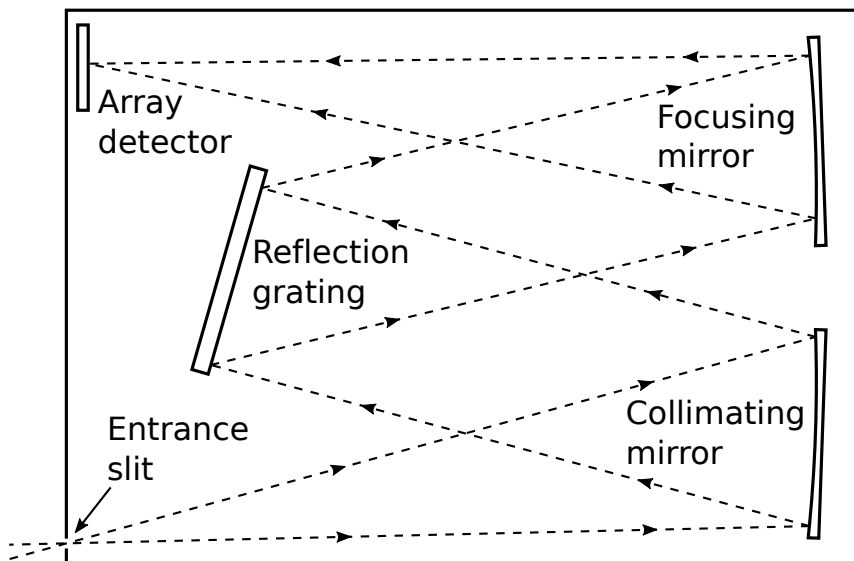


Figure 3.7: Simplified drawing illustrating the principles Czerny–Turner grating spectrometer. Light enters the spectrometer through a slit and is collimated by a concave mirror. The collimated light is reflected onto a reflective blazed diffraction grating which produces wavelength dispersion. The dispersed light is then focused onto an array detector by a second concave mirror.

convolution of a boxcar function caused by the finite width of the entrance slit and a more complicated lineshape function caused by the finite number of slits illuminated on the grating. The instrumental lineshape and the wavelength-to-pixel mapping on the array detector is normally determined by measurement of thin emission lines from a well known calibration source, such as a low-pressure mercury vapor lamp [25].

3.4.2 Spectral retrievals

A large number of species can potentially be measured with DOAS. However, as for SOF, the number of species typically encountered with large enough columns from industries to be measurable with Mobile DOAS is limited. Mobile DOAS has successfully been used to measure volcanic SO_2 emissions [26], emissions of SO_2 , NO_2 and HCHO from industrial areas [27, 28] as well as from entire cities [29–33]. The Mobile DOAS results presented in Paper II and Paper III are all based on spectral retrievals of SO_2 , NO_2 and formaldehyde (HCHO) from spectra measured in the wavelength interval 310–350 nm. SO_2 has been retrieved

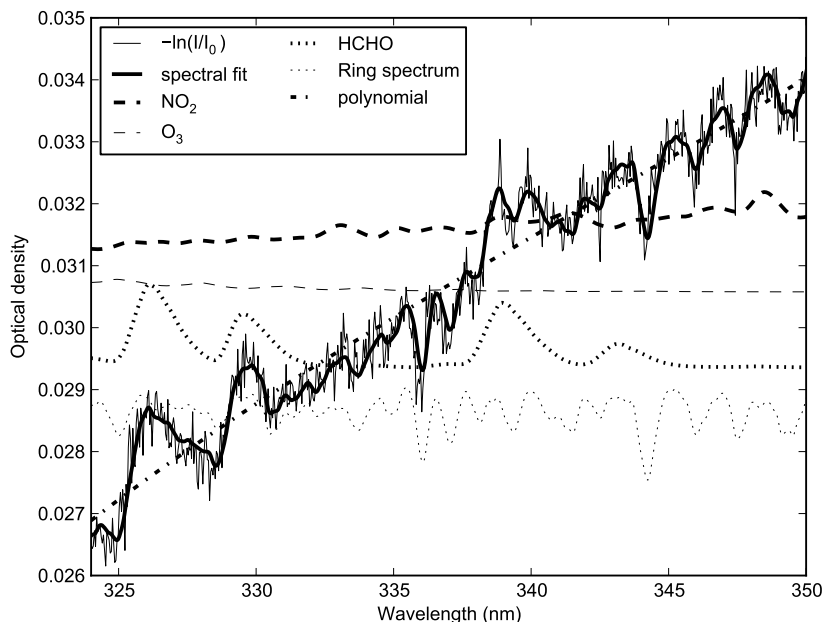


Figure 3.8: Spectral fit in the 324–350 nm retrieval window used for retrieval of NO_2 and formaldehyde (HCHO) columns. The plot shows the measured and fitted absorbance, as well as the individual components of the fit. All the individual components except the polynomial have been shifted in the y-direction for the purpose of visual display. $(\text{O}_2)_2$ was not included in the plot since it was negligible in size.

in the 310–325 nm window, while NO_2 and formaldehyde have been retrieved in the 324–350 nm window. In Paper **IV** a 336.5–359 nm fitting window was used for retrieving NO_2 and HCHO instead. Apart from the species of interest, the spectral retrievals have included two cross sections of O_3 , one at 223 K and one at 293 K, one for the $(\text{O}_2)_2$ collision complex, and a synthesized Ring spectrum. The two cross sections for O_3 are needed to fit the absorption of both stratospheric and tropospheric ozone. The stratospheric column, however, is too large to allow quantification of the tropospheric ozone from this retrieval. The $(\text{O}_2)_2$ collision complex is a hypothetical short-lived complex formed from collisions of oxygen molecules. It has never been detected chemically. The only evidence for its existence is a number of spectral absorption bands that are proportional to the square of the oxygen concentration. Even though it is proportional to the square of the concentration, the cross section can still be used in the spectral retrieval as a normal cross section, but the physical interpretation of it will be slightly different. The retrieved column of $(\text{O}_2)_2$ can be used as an indicator of problems with multiple scattering. If the light that passes through a plume

follows a similar path as the reference, there should not be a large differential $(\text{O}_2)_2$ column between them. If there is significant multiple scattering in the plume, however, the total path length of the light will be different and the light will therefore pass through more $(\text{O}_2)_2$. A sudden large change in $(\text{O}_2)_2$ when passing through a plume is hence a sign of multiple scattering in the plume. Figure 3.8 illustrates a spectral fit in the the 324–350 nm window. In this spectral fit, the reference was taken shortly before the evaluated spectrum. This explains why the O_3 and $(\text{O}_2)_2$ component are so small.

3.4.3 Radiative transfer modeling

As described in section 3.2, the result of a spectral retrieval is in the form of columns, or differential columns, which are defined as the integral of the concentration along the light path of the measured light. However, due to scattering there are an infinite number of possible paths that the light can take through the atmosphere before reaching the instrument. Since it is likely that not all the light measured has taken the same path, the retrieved column may be thought of as the average column among all paths taken (assuming that the absorption is optically thin). For a given measurement situation we may define the *air mass factor* A as [34]:

$$A = \frac{S}{V}, \quad (3.35)$$

where S is the column measured in this situation, usually referred to as *slant column*, and V is the *vertical column*, i.e. the concentration integrated along a vertical path. The vertical column is a physical quantity that is independent of the specifics of the measurements and the air mass factor may be thought of as a weighting factor describing the magnitude of the impact of V on the measured column. Air mass factors can be defined for the full atmosphere, or for specific layers. If the atmosphere is divided into a large number of smaller layers and an air mass factor is defined for each, these are known as *box air mass factors* or *weighting functions*. For direct sun measurement, as used for SOF, the fraction of light taking other paths than the straight path from the sun to the instrument is generally negligible, and hence the air mass factor for the whole atmosphere can be assumed to be $1/\cos\theta$, where θ is the solar zenith angle (SZA). For DOAS measurements of scattered sun light, on the other hand, it is not as simple. All the light measured has been scattered at least one time so it cannot be assumed that scattering is an insignificant effect. In many situations the *geometrical* approximation [34] is used. In this approximation the air mass factor for the stratosphere is assumed to be $1/\cos\theta$ and the air mass factor for the troposphere is assumed to be $1/\cos\theta_V$, where θ_V is the viewing zenith angle. This approximation would imply that most of the light has been scattered only once and that most of those scattering events took place somewhere in the boundary region between the troposphere and the stratosphere.

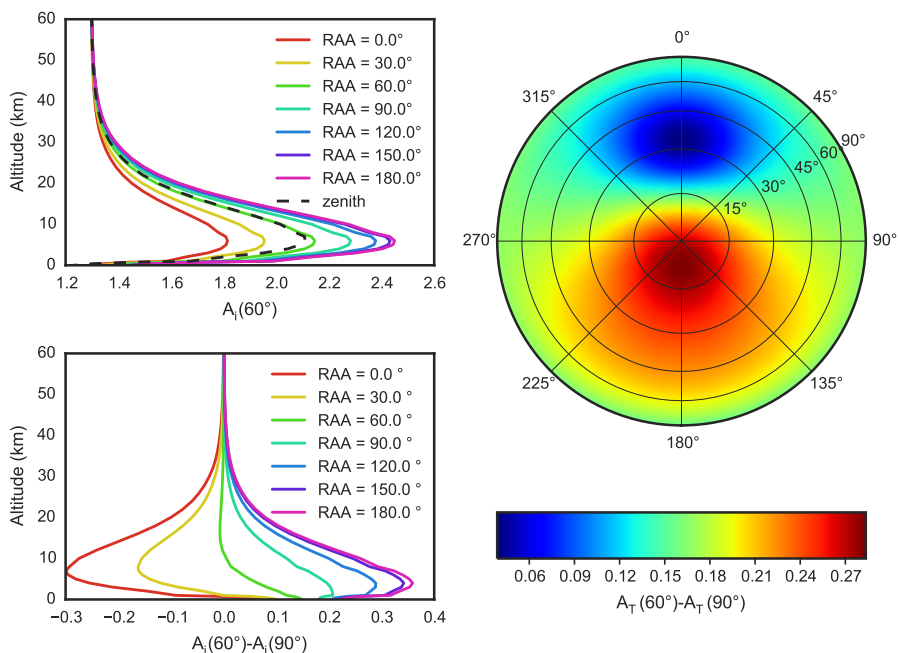


Figure 3.9: Example of air mass factors calculated from radiative transfer simulations. The top left panel shows box air mass factors for different azimuthal angles relative to the sun, the bottom left panel shows the difference between the box air mass factors for two different viewing zenith angles, again for different azimuthal angles. The right panel shows the difference in tropospheric air mass factor for NO₂ between the two viewing zenith angles as a function of solar zenith angle (radial axis) and azimuthal angle (angular axis), as calculated from the box air mass factors.

Another approach is to use a radiative transfer model to simulate how the solar light propagates through the atmosphere for a particular scenario defined in terms of trace gas concentration profiles, aerosol loadings, solar zenith and azimuth angle, viewing direction, etc. There are a number of radiative transfer modeling softwares available and many of them allows air mass factors to be calculated as the direct output of the simulations. For Paper IV box air mass factors were calculated using the radiative transfer modeling software package SCIATRAN [35] which solved the radiative transfer using the discrete-ordinates method. An example of the results from these simulations is shown in figure 3.9.

Although the geometrical approximation has been used in most Mobile DOAS flux measurements so far [26, 27, 29–31, 33, 36–38] it may be noted that this is associated with an extra source of uncertainty in comparison with direct sun measurements, such as used in the SOF method. Air mass factors could also be calculated for flux measurements, but these may not be directly applicable

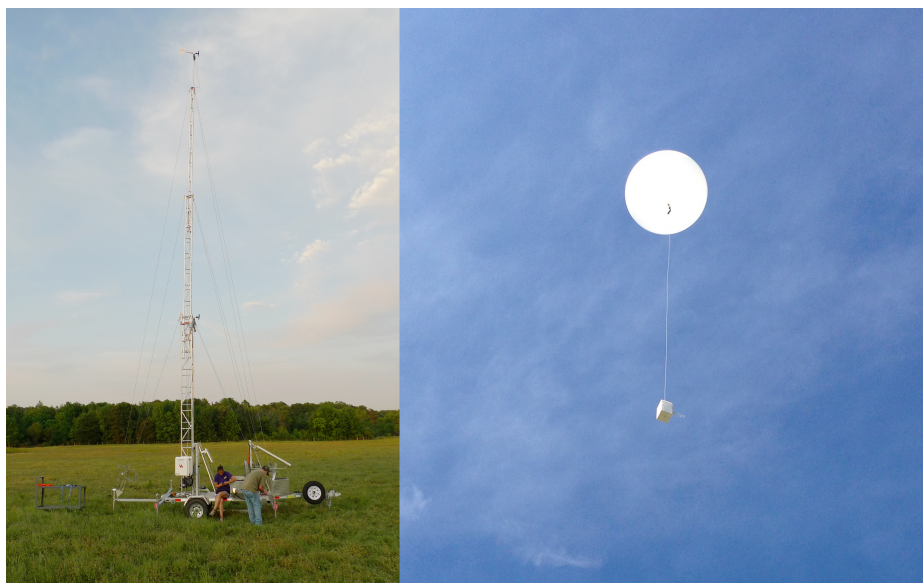


Figure 3.10: A portable 15 m wind mast deployed in open field with anemometers at two heights (left picture) and a GPS-tracking radiosonde that has just been launched into the air with a helium balloon (right picture).

to measurements of small scale plumes since there is an implicit assumption of horizontal homogeneity in the normal application of air mass factors.

3.5 Wind measurements

As discussed in section 3.2, flux measurements with SOF and Mobile DOAS are fundamentally dependent on accurate wind velocity information. The wind velocity used in equation (3.28) should ideally be the mass-weighted average of the wind velocity of the gas measured in the plume cross section. This velocity is typically not possible to measure directly. Instead the goal must be to make wind measurements that are as representative as possible of the average velocity of the plume. A number of methods for wind measurements exist and are described below.

3.5.1 GPS radiosondes

A GPS radiosonde is a small electronic device powered with batteries. Its electronic components include a GPS (Global Positioning System) receiver, a radio transmitter, and various other sensors, such as temperature, pressure and relative humidity sensors. The sonde is launched from the ground with a large helium balloon and rises through the atmosphere with an ascent rate of a few meters per second. During the flight, the radiosonde sends its GPS position and other measurement data to a receiver on the ground, which logs the data. The

balloon and radiosonde are assumed to follow the local horizontal wind field as they rise through the atmosphere, enabling a height profile of the wind velocity to be reconstructed by differentiating the horizontal position of the sonde with respect to time. A radiosonde attached to a helium balloon that has just been launched is shown in the photo on the right in figure 3.10. The radiosondes used can easily reach altitudes well into the stratosphere and the additional sensors also give temperature, pressure and humidity profiles, but for the purpose of flux measurements, only the wind velocity profile in the boundary-layer, typically from ground up to 500–2000 m in fair weather, is of interest. Figure 3.11 shows the wind speed and wind direction profiles obtained from two radiosonde launches from a measurement campaign in Longview, Texas in May 2012. Each launch usually takes 5–10 minutes and gives a snapshot of the wind profile at that time. Since the radiosonde and balloon is lost in each launch, the number of launches during a measurement campaign is often limited by budgetary constraints. For this reason, wind profiles measured with radiosondes sufficiently close in time are not always available for all flux measurements. For the purpose of flux calculations, the wind velocity is typically averaged over a height interval assumed to be representative of the height distribution of the gas in the plume. Height intervals used have been 0–200 m, 0–350 m, and 0–500 m. The averages calculated for these intervals have also been used as benchmarks for other measurements.

3.5.2 Ground-based wind masts

Anemometers of different design, such as cup, windmill or sonic anemometers, mounted at the top of a weather mast provide the cheapest way to make continuous wind measurements. Fixed installations of weather masts, operated by various organizations, often exist in many industrial locations, or in the vicinity. This wind data can often be obtained for free from the operator. A mobile mast can also be deployed at a suitable site. An example of a 15 m high mobile mast deployed in an open field is shown in the photo on the left in figure 3.10. The problem with these wind measurements is that the wind field is more disturbed and turbulent closer to the ground. This means that the wind measurements from masts often significantly underestimate the wind speeds higher up, and are subject to larger random variations. The magnitude of these effects depend on the height and location of the mast, the surrounding topology, the speed and direction of the wind, etc. A higher mast means that the anemometer is further from the ground and the measurements suffer less from these effects, but higher masts are also more expensive and therefore less commonly available. To compensate for the systematically lower wind speeds measured by a mast, height interval averages of a large number of radiosonde profiles can be compared to averages of the wind velocity measured by the mast during the same time interval. A scaling factor for the wind measured by the mast can then be determined so that they match on average. The flux calculations presented in Paper I, Paper II and Paper III have been made using radiosonde profiles when available sufficiently close in time, and mast measurements scaled to remove systematic

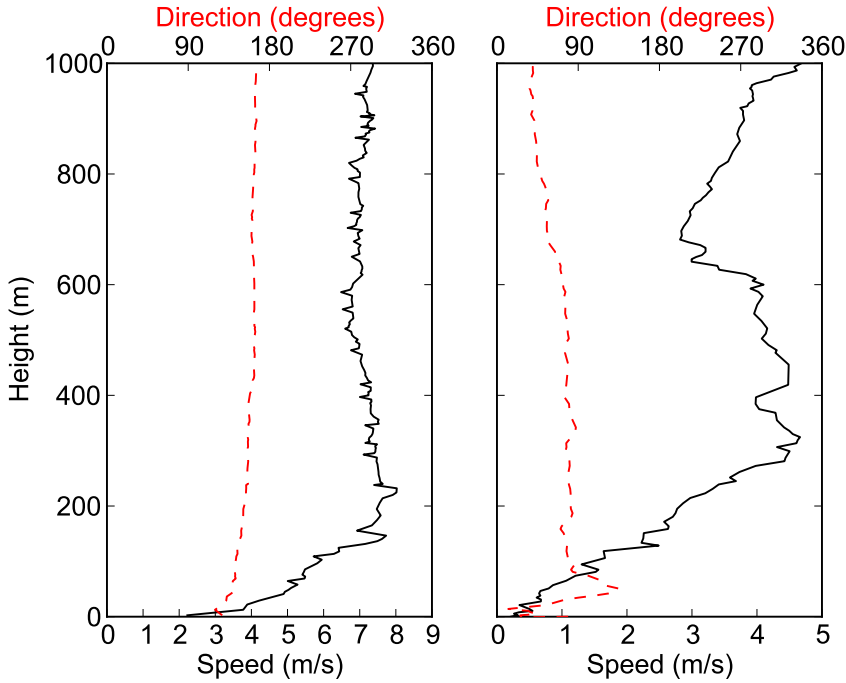


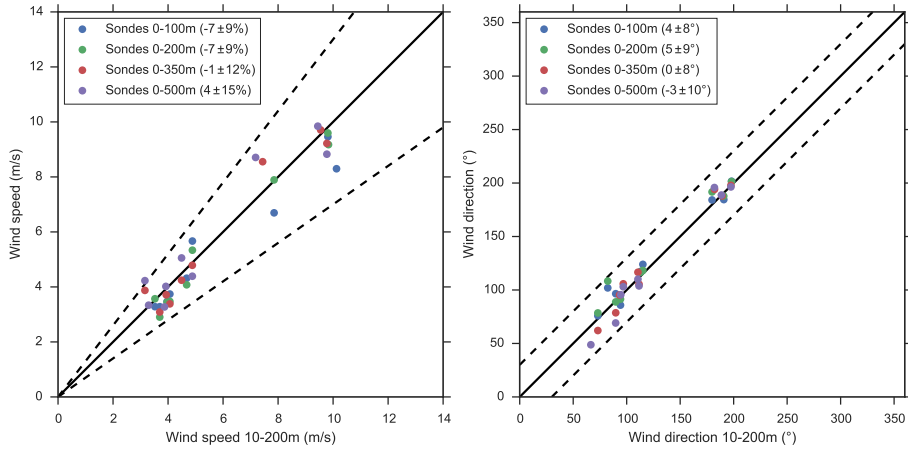
Figure 3.11: Two wind velocity profiles measured with radiosonde launches. The first wind speed profile is nearly constant over height with only a small decrease closest to the ground, while the second shows considerably more variation.

differences compared to such radiosonde profiles at other times.

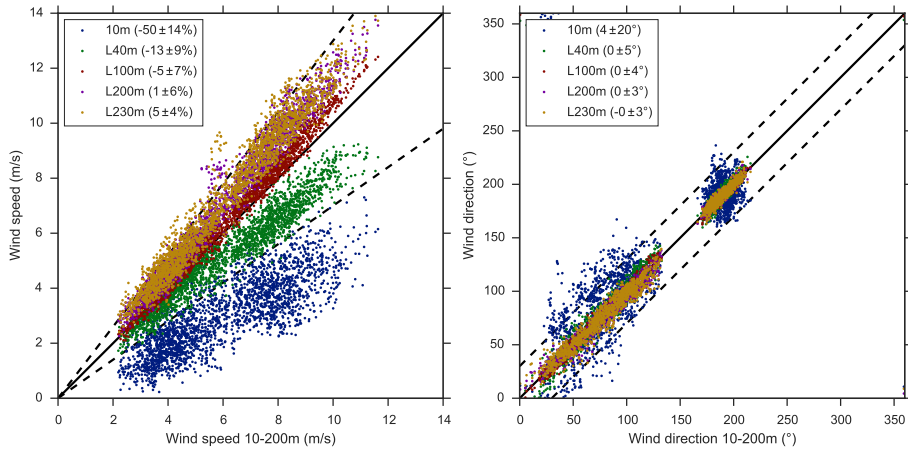
3.5.3 Remote sensing wind profilers

Remote sensing wind profilers in theory present the perfect combination of the advantages of both radiosondes and wind masts. They measure height profiles of the wind velocity continuously. The most common principle for this is to send a signal up into the atmosphere and measure the Doppler shift of the backscatter signal. This is typically done in a number of different directions to be able to calculate the different components of the wind. During a few SOF and Mobile DOAS measurement campaigns, wind profile data measured with radar and/or sodar profilers have been available. Radar profilers use electromagnetic waves in the radio frequency region, while sodar profilers use sound waves. However, these data generally had low availability and/or large errors compared to simultaneous profiles measured by radiosondes. For this reason, they have not been used for flux calculations. To what extent these problems are inherent to the methods or just to the specific instruments or their operation is unclear.

In recent years, a third remote sensing wind profiling method, wind lidar, has



(a) Wind lidar vs. radiosondes



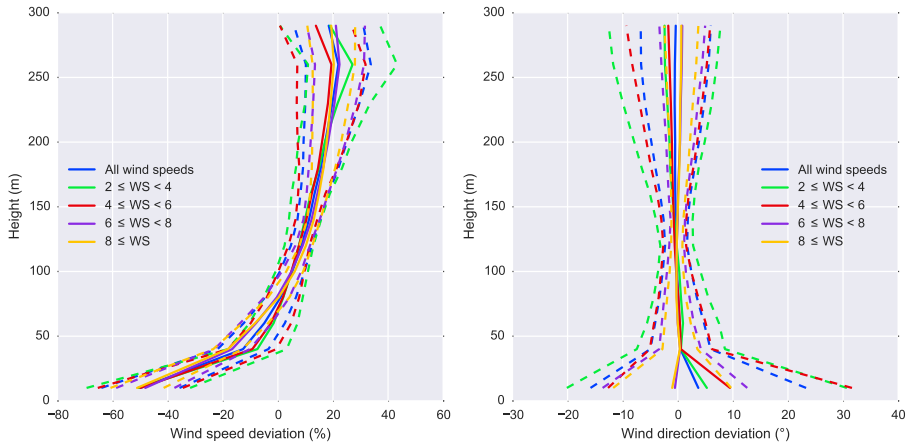
(b) Wind variability by height

Figure 3.12: Intercomparisons of wind measurements by wind lidar and radiosondes, and the variability of wind lidar data by height. (a) Comparison between 0–200 m averages of wind profiles measured with radiosondes on the y-axis, and 0–200 m averages of simultaneous wind profiles measured with a wind lidar located at the radiosonde launch site on the x-axis. Dashed lines indicate $\pm 30\%$ for wind speeds (left panel) and $\pm 30^\circ$ for wind direction. (b) Comparison between 0–200 m 5 minute averages of wind profiles measured with wind lidar on the x-axis, and simultaneous 5 minute averages of winds at specific heights within that interval (and one outside). The 10 m wind is measured with a ground mast while all the other heights are measured by the same lidar as the 0–200 m average. Dashed lines indicate $\pm 30\%$ for wind speeds (left panel) and $\pm 30^\circ$ for wind direction.

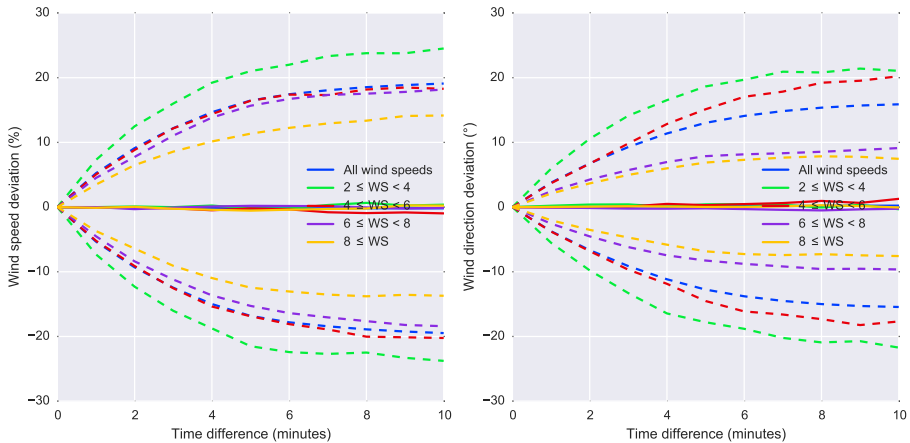
become more widely available and has demonstrated high measurement accuracy [39]. A wind lidar sends out a near-infrared laser beam and detects the Doppler shift of light backscattered by aerosols in the air mass above it. By either using a pulsed signal and measuring the shift as a function of return time, or by sequentially focusing on different distances, the wind lidar can determine the wind speed along the measurement direction at a number of distances away from it. By repeatedly performing such measurements while scanning the measurement beam in a conical pattern, a vertical profile of three-component wind velocity vectors can be reconstructed. In recent flux measurement studies, wind lidars have been included in an effort to improve wind speed accuracy and to gain a better understanding of wind variability. Figure 3.12 shows the result of a comparison between wind data from radiosondes and a wind lidar positioned at the radiosonde launch site, as well as comparisons of winds at different heights measured by the lidar simultaneously. The data comes from over a week of measurements during typical SOF conditions. The radiosonde-to-lidar comparison indicates very good agreement. The wind speed shows less than 10% systematic difference for 9 radiosonde launches regardless of whether they are averaged from ground to 100, 200, 350 or 500 and the systematic difference in direction is similarly 5° or less. The comparison of different measurement heights of the wind lidar confirms the picture of little systematic variation by height above 100 m but shows that there can be steep gradient at lower heights. A 10 m wind mast included in the comparison showed on average 50% lower wind speeds and significantly more random variation, while the 40 m lidar wind speed was on average 13% lower. Figure 3.13 illustrates in a different way how wind varies with height and time, as well as how that variation differs between different wind speed ranges. This figure illustrates clearly that the random wind variability is higher in the lower wind speed ranges than in the higher. This would indicate that flux measurements would be more accurate in stronger winds. On the other hand, stronger winds normally leads to lower columns which may increase the relative uncertainty of the spectroscopic measurements.

3.6 Plume height estimation

The wind speed used for flux calculations should ideally be the average speed of the gas in the emission plume of interest. Since wind speeds tend to vary with height, due to ground retardation, the height distribution of the plume is an important parameter to consider when assigning plume speed for the flux calculations. In situations with steep height gradients in the wind speed and narrow plumes, the potential for error due to assumptions about plume height increases. Fortunately, the conditions needed for SOF measurements, clear and sunny weather, are typically associated with strong convection which causes fast vertical mixing in the boundary layer. This leads to a smoothing effect on vertical gradients in both wind speed and plume concentration, which mitigates this problem. The longer the plume transport time is, the more mixed the plume will also be. The strongest vertical wind gradients are normally found within



(a) Wind variability by height and wind speed



(b) Wind variability by time and wind speed

Figure 3.13: Wind variability with height and time for different wind speed ranges based on 5 minute averages of measurements by a wind lidar and a 10 m high mast. (a) Deviation at specific heights from 10–200 m average. Solid lines indicate mean and dashed lines indicate standard deviation. Different colors indicate different wind speed ranges. (b) Deviation of the 10-200 m average wind from the same average with a time offset. Solid lines indicate mean and dashed lines indicate standard deviation. Different colors indicate different wind speed ranges.

the first tens of meters from the ground. For flux measurements with SOF and Mobile DOAS, the plume is usually assumed to be well-mixed up to a height of at least 100 m. At heights above this, systematic wind speed gradients are typically small and hence the average wind speed from ground to 100 m is not normally very different from the average from ground to for instance 300 m. If the measured plumes were instead mostly confined within the first tens of meters above ground, this approach would have larger uncertainties and the flux would most likely be overestimated. For this reason it has been important to test the assumption of plume mixing heights. One approach used to estimate the plume height is to measure the in situ ground concentration of a species simultaneously with SOF measurements of the columns of the same species in a plume. Such measurements have been performed a few times using mobile extractive FTIR spectroscopy (MeFTIR) for the ground concentration measurements. MeFTIR is based on similar spectroscopy to that of SOF, but using an artificial light source and a multi-pass (White) cell to achieve a long light path within a small cell [40].

In an idealized situation where ground mass concentration ρ of a species is measured by MeFTIR, the mass column S of the same species is measured simultaneously with SOF and the concentration can be assumed to be constant along the light path up to height H where it drops to 0, they would follow this relationship

$$S = \frac{\rho H}{\cos \theta}, \quad (3.36)$$

where θ is the solar zenith angle. In this case H could be computed as

$$H = \cos \theta \frac{S}{\rho}. \quad (3.37)$$

For a realistic emission plume, however, this assumption will not hold true. Still a relatively robust plume depth (or plume height) estimate can still be calculated by integrating the measured concentrations and columns along the measurement path as the plume is transected. The plume depth estimated is then given by

$$H_e = \cos \theta \frac{\int S(x) dx}{\int \rho(x) dx}, \quad (3.38)$$

where the integration variable x is the cross-plume distance driven by the measurement vehicle. Figure 3.14 shows four examples of what the concentration of a species may look like in the cross section of an emission plume. Example 1 is a very idealized case with a uniform concentration in a rectangular cross section. For this example H_e would actually represent the upper edge for the rectangle and would be a very accurate estimate of the plume depth. In reality plumes

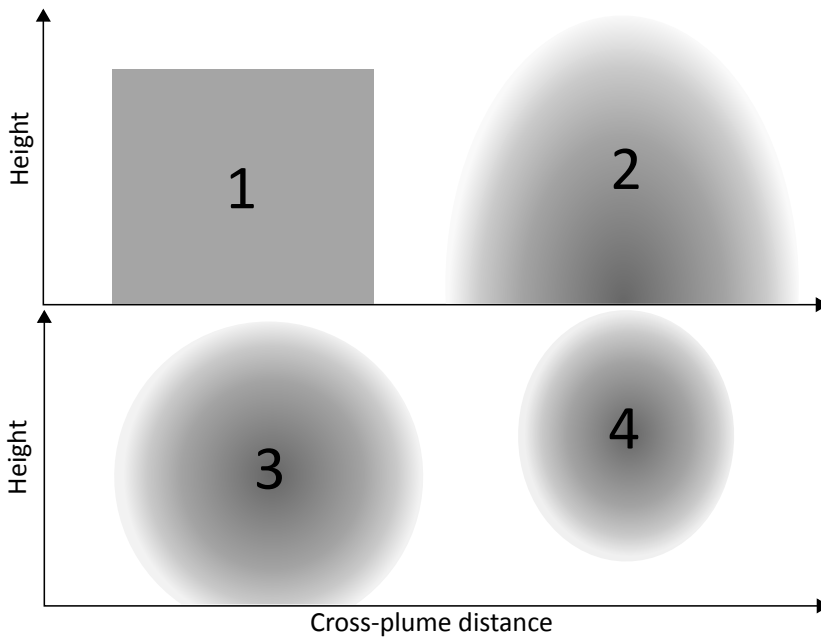


Figure 3.14: Four examples of what the concentration distribution of an emitted species might look like in a plume. Darker shades of gray indicated higher concentrations. Example 1 is an idealized case for which the plume depth estimate is strictly true. Example 2 is a typical example of where the plume estimate is not strictly true but still gives a reasonable estimate. Example 3 represents a case with an elevated plume partially dispersed to the ground for which the plume depth estimate may produce a significant overestimate. Example 4 shows a completely elevated plume for which the plume depth estimate cannot be calculated.

tend to form a more Gaussian distribution as they disperse in the atmosphere. Example 2 might represent the distribution of a plume from a ground source at a medium distance. In this case H_e would be lower than the highest reach of the plume, but the height range 0 to H_e would still be a good estimate of where most of the plume is located, and hence the average wind for this height range would generally be representative of the average plume velocity. The most problematic case is shown in example 3. Here an elevated plume has partially dispersed down to the ground, but the ground concentrations are still much lower than what can be found further up. In this case H_e might significantly overestimate the extent of the plume. Finally, example 4 shows an elevated plume that has not been dispersed down to the ground at all. In this case H_e cannot be calculated, but it will be apparent from the lack of ground plume that this is an elevated plume. Example 3 shows that there are cases where this plume depth estimate can be misleading, but these types of situations are probably unusual, since it is an

intermediate situation as an example 4 plume transitions to something that is more like example 2.

Figure 3.15 shows an example of simultaneous column and ground concentration measurements downwind of two large refineries as well as height estimates H_e calculated according to equation (3.38) for a number of different segments of the transect. For the full width of each of the two broad plumes, the plume height estimates are well above 300 m (indicated by dashed lines), but for a part of the plume from one of the refineries, the plume estimate is only slightly above 100 m. Repeated plume height estimates of this type have been performed within a couple of measurement studies and they have indicated that the plume height in most cases is at least above 100 m. In a few cases, the plume height has been slightly below 100 m for parts of a plume, but only in single a case, where the measurement route was unusually close to emission source, has it been below 50 m. Based on this the assumption of vertical mixing of emission plumes up to at least 100 m has been considered realistic for typical SOF and mobile DOAS measurements.

3.7 Error analysis

There are a number of different potential error sources for flux measurements with SOF and Mobile DOAS. In assessing them it is important to distinguish between systematic errors and random errors. Normally, several flux measurement are made on the same source and an average flux is calculated. If there is an uncorrelated random error with standard deviation σ in each flux measurement and the average of N such measurements is calculated, the error in the average will be σ/\sqrt{N} . For systematic errors, on the other hand, the size of the error does not decrease with the number of measurements. The potential error sources for flux measurements are listed below.

3.7.1 Spectroscopic errors

These are errors in flux measurements due to errors in spectroscopically determining the column along the measurement path.

Uncertainty in strength of cross sections

The cross section that have been used for SOF and Mobile DOAS have been measured and published by other groups. Cross sections are generally published together with an estimated uncertainty for the absolute strength. For VOC measurements with SOF, cross sections from PNNL (Pacific Northwest National Laboratory) [41], with reported uncertainties in the range 3–3.5%, have been used. For Mobile DOAS, cross section from Bogumil [42], Vandaele [43] and Cantrell [44] have been used for SO_2 , NO_2 and formaldehyde respectively. Their reported uncertainties are 2.8%, 4% and 3% respectively.

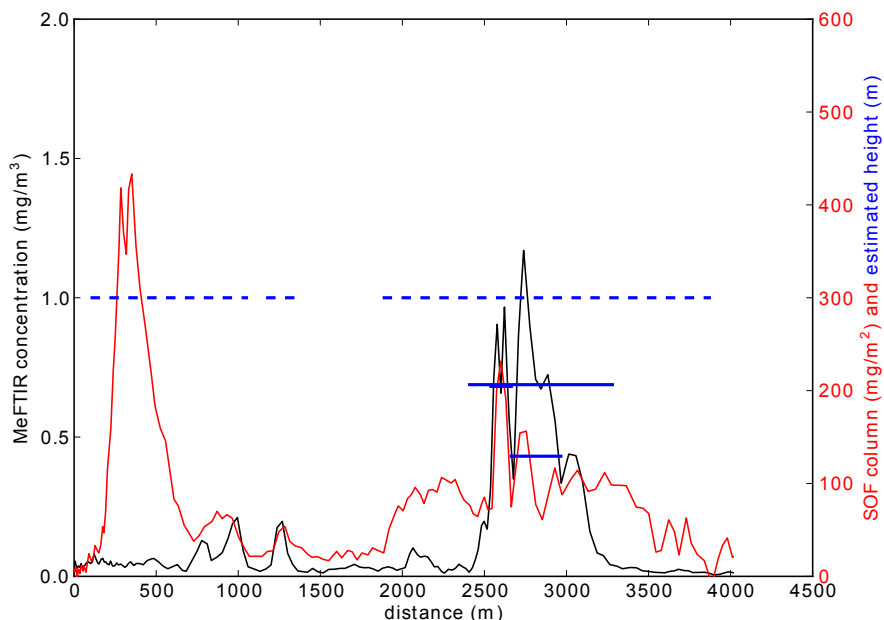


Figure 3.15: Example of simultaneous SOF alkane columns measurements (red) and MeFTIR alkane ground concentration measurements (black). The blue lines indicate plume height estimates calculated for various segments of the measurement transect. The dashed blue lines at 300 m indicate that the plume height estimate was higher than 300 m.

Retrieval errors

No spectral retrieval routine can fit the measured absorbance spectra perfectly. There will always be a residual left that could not be fitted. The residual has two types of causes, measurement noise and residual structures. Measurement noise will exist in any spectral measurement. In FTIR measurements detector noise is the dominant noise source, while in UV measurements with a CCD detector, statistical photon noise, also known as shot noise, will typically dominate. Both of these can approximately be described as uncorrelated Gaussian noise. For detector noise the signal-to-noise ratio is proportional to the light intensity, while for shot noise it is proportional to the square root of the intensity. If measurement noise is the only cause of the spectral fit residual, the residual will be mostly noise. Each fitted cross section will, however, receive some random interference from the noise, adding a random error to the evaluated columns. This error will also be a random uncorrelated error, whose magnitude can be statistically estimated from the magnitude of the residual noise and the strength of

the cross section in the evaluation window. However, a simpler way to estimate the magnitude of the random column errors is to look at the random variations in evaluated column before or after passing the plume. The latter method is typically used to assess the random retrieval error.

Residual structures can be caused by any phenomenon affecting the measured spectra in a way that the spectral fitting routine cannot properly account for. Potential sources are unknown absorbers, scattering, changes in the instrument, non-linearity effects etc. These will generally produce residual components that are not noise, but instead have some non-random spectral structure. The effect of these on evaluated columns is more difficult to quantify. The effect will also generally not be a random error, but instead errors in consecutive measurements will be correlated. Some effects may cause a steady predictable drift in evaluated columns, while others may just affect the measurements temporarily, causing a bump in the column time series.

3.7.2 Wind measurement errors

The largest source of error in flux measurements is generally the wind measurements. This is not primarily a measurement error, in the sense that the measured wind velocity is wrong, but in the sense that it is not representative of the wind velocity in the plume. This is mainly due to that the wind is not measured in the same location and/or at the same time as the gas in the plume. This could cause both systematic and random errors in both wind speed and wind direction.

Wind speed errors

The main cause of systematic errors in wind speed is vertical wind gradients. These are caused by the wind field closer to the ground being retarded by the friction of the ground. This effect is somewhat mitigated by convection, which causes vertical mixing and smoothing of the vertical gradients. SOF and Mobile DOAS measurements are generally made during clear weather, associated with strong convection. Comparisons of averages of radiosonde wind speed profiles over the intervals 0–100 m, 0–200 m and 0–500 m were made for three different launch locations used in a measurement campaign in Houston in 2009 [45]. The wind speed in the interval 0–200 m was on average -3% , -9% and $+2\%$ compared to the 0–500 m interval for the three different launch sites. The same comparisons between the 0–100 m interval and 0–500 m showed average differences of -2% , -15% and -1% . During another campaign in Houston in 2006 [46] a similar comparison was made between the intervals 0–200 m and 0–500 m and the wind speed was found to be on average -6% in the former compared to the latter. If these height intervals are thought to be representative of the variations in vertical extent among plumes measured with SOF and Mobile DOAS, the systematic error due to not knowing the true plume extent will most likely be less than 10%.

The systematic difference between profile averages and winds measured by wind

masts on the ground is often much larger, up to 30–40%. This is because the masts are so close to the ground in comparison. Most masts used in the Texas campaigns have been 10–20 m high. Emission plumes are however rarely confined to such low heights during daytime on sunny days. The same convection that smooths vertical wind gradients also causes rapid vertical mixing of the plume. Studies have showed typical vertical mixing speeds of 0.5–1.5 m/s [47]. For this reason, wind speeds measured by wind masts have been scaled to remove systematic differences compared to a radiosonde wind profiles in a chosen height interval, often 0–500 m. The remaining variation between profile averages and scaled wind mast speeds typically has a standard deviation of 15–30%. Random errors can potentially be reduced by performing multiple measurements, but that is dependent on the random errors being uncorrelated. This might not always be guaranteed. If a certain type of wind measurement underestimates the speed of a plume during one measurement, it is probably likely to do so again if another measurement is made directly afterwards, but not if another measurement is made the next day. The random errors probably have some typical correlation scale, both in terms of time difference and distance. Since measurements are often made close in time after one another, the random error cannot necessarily be expected to be reduced by a factor of \sqrt{N} . For this reason the random error is used as a conservative estimate of the remaining wind speed error even after averaging several measurements.

Wind direction errors

Systematic differences in wind directions may exist between different heights, although these differences are often less consistent than for wind speed. For wind masts on the ground there could be additional systematic errors in wind direction due to the local surrounding. The effect of wind direction errors on flux measurements is, however, not as straightforward as for wind speed. The wind direction enters the flux calculations, see equation (3.28), in the form of the factor $\sin(\alpha_j)$ where α_j is the angle between the wind direction and the driving direction of the measurement vehicle. An error in the wind direction will carry over to an error in α_j , but its influence on the $\sin(\alpha_j)$ will be highly dependent on α_j . To estimate this effect, the average absolute error in wind direction has first been estimated by comparing wind mast measurements to radiosonde profiles, as done for the wind speed. The average absolute error for different wind masts has generally been in the interval 10–20°. The effect of this error has been approximated for different true values of α_j by simulations assuming a Gaussian distribution of wind errors with standard deviation given by the average absolute errors of the wind masts. For $\alpha_j = 90^\circ$ these simulations have shown average absolute flux errors in the range 4–8%, while for $\alpha_j = 75^\circ$ this error has been in the range 8–12%. This is a random error but as for the random wind speed error it cannot be assumed to be uncorrelated. For this reason 4–12% is a reasonable conservative estimate of the flux measurement error due to wind direction error. In many cases the larger wind speed errors can be avoided due to geometric constraints. If the location of the emission source is known, a straight line from

the center of it to the center of the measured plume cross section should be a fairly good approximation of the wind direction. Measured wind directions that deviate too much from this should be avoided, either by choosing another wind source or by setting the wind direction manually. This practice should reduce the average wind direction error. This effect has, however, not been included in the estimate of the wind speed error.

3.7.3 Other error sources

Background variations

In the ideal flux measurement the measured species are not present in the background atmosphere, and if they are, their concentration should at least be constant during the measurement. This is, however, not always the case. Background concentration can change due to upwind emission sources or changing air mass transport. This will cause deviations in the evaluated columns that are not due to the emissions in the plume. Furthermore, changes in the light path of the measured light can result in a longer or shorter path through a constant background concentration, also causing deviations in the evaluated columns. For SOF this change in light path is due to the movement of the sun, while for Mobile DOAS it is due changes in where light is scattered from. In many ways the effects of background variations are similar to those of residual structures. For this reason, they can be treated together. Both residual structures and background variations can sometimes result in steady, continuous increases or decreases in the evaluated columns. These can sometimes be compensated for by making a slant background correction, i.e. subtracting a linear function, or even a higher polynomial in some cases, from the column time series. But not all variations are steady and continuous. Sometimes these effects can cause large irregular baseline variations which cannot be compensated for. The relative error in a flux measurement due to baseline variations will depend on the size and type of the variations, the magnitude of the flux measured, and the width of the plume. The size of this error is generally limited by exclusion of measurements where the baseline variations would cause a too large error. For each flux measurement a baseline is established manually. If this cannot be established with reasonable certainty in relation to the magnitude of the plume peak, the measurement is rejected. Similarly, the measurement can also be rejected if the retrieval noise is too large in relation to the plume peak. It is estimated that this practice, as it has been applied, can limit the error due to baseline variations and retrieval noise to less than 10%.

Plume meandering

The flux calculation formula assumes a stable plume remaining in the same place for the entire measurement. In reality the plume might often meander back and forth along the measurement route. The gas in the plume is primarily moving in the direction of the plume, not in the direction the plume is meandering. The drift of the plume is an apparent movement, caused by subsequent segments

of the plume having been affected by slightly different wind fields, and thereby having traveled along different trajectories. If this apparent plume drift is in the same direction as the measurement vehicle is driving, the plume will appear wider than it is, and if it is in the opposite direction it will appear narrower. If the measurement vehicle is driving with speed v and the apparent plume drift speed parallel to the driving direction is u , the ratio between the calculated flux F_c and the true flux F_t will be:

$$\frac{F_c}{F_t} = \frac{v}{v - u} = \frac{1}{1 - \frac{u}{v}}. \quad (3.39)$$

If u is small compared to v this can be approximated by:

$$\frac{F_c}{F_t} = 1 + \frac{u}{v}. \quad (3.40)$$

Hence, the relative error in the flux calculation is u/v for small u . This assumes that the apparent plume drifts in the same direction with the same speed for the whole measurement. If it drifts back and forth within the time of one measurement, the effects will cancel and the error will be smaller. In the long run, a plume should be expected to drift equally in both directions. If several measurements are made on the same plume, drift along the driving direction should be equally likely as drift in the opposite direction. Hence, this error is assumed to be a random and uncorrelated error. Therefore, its magnitude should decrease with averaging of a large number of measurements. It is not known what typical drift speeds of plumes might be, but the effect is assumed to be small due to the moderate variations in flux typically seen between measurements and because of averaging.

3.7.4 Composite flux measurement error

The different error sources described above are assumed to be uncorrelated with each other and can therefore be combined to a composite flux measurement error, σ_c , by root-sum-square:

$$\sigma_c = \sqrt{\sum_i \sigma_i^2}, \quad (3.41)$$

where σ_i are the estimated standard deviations of the different error sources. In root-sum-squares the largest components tend to dominate, which for σ_c means that the wind speed error tends to be the most important. A wind error analysis has generally been made for each measurement campaign and a composite error or error interval has been calculated based on this. These values for σ_c have typically been in the range 20–40%. This error represents the error of an average of a number of measured fluxes compared to the average of the true fluxes at

the times of those measurement. When using an average of measured fluxes as an estimate of emissions during a certain time period, there might also be sampling errors due to emissions at the times of the measurements not being representative of the time period.

4

Summary of papers

4.1 Measurements of industrial emissions of alkenes in Texas using the solar occultation flux method

This paper presents the Solar Occultation Flux (SOF) method and its application to measure industrial alkene emissions. Results from SOF alkene measurements during the Second Texas Air Quality Study (TexAQS II) in 2006 are presented, both as a demonstration of the capabilities of the method, and to compare to emission inventories. SOF measurements of total emissions of ethene and propene from 7 sectors of Houston Ship Channel (HSC) as well as from the surrounding industrial areas in Bayport, Channelview, Chocolate Bayou, Freeport, Mont Belvieu, Sweeny and Texas City are presented and compared to emission inventory data for the corresponding areas. The geometrical average of the ratios between measured and inventory emissions for the different areas was 10.2 (+8, -5) for ethene and 11.7 (+7, -4) for propene. The two largest sources of alkene emissions were HSC and Mont Belvieu which had combined average measured ethene and propene emissions of 1250 ± 180 kg/h and 2140 ± 520 kg/h respectively. The corresponding 2006 inventory emissions for these areas were 145 and 181 kg/h.

Emissions from the area around Battleground Road were studied in detail due to their large temporal variations. In an episode on August 31, 2006, measured emissions rose from 684 to 2295 kg/h within 30 minutes, and then fell to only 237 kg/h within another 30 minutes. Hourly emission inventory data based on in-situ measurements showed large short-term variations in emissions from flares in this area, but these could not be shown to correlate exactly with the temporal

variations in emissions measurements. Still, the hourly inventory measurements showed the potential for large short-term variation in flare emissions, and not all flares in the area were included in the hourly inventory. Furthermore, the hourly inventory data for flares was based on the assumption of 98–99% combustion efficiency, and further large-scale variations might be expected if this assumption did not hold.

In a number of cases, emissions of alkenes were also estimated based on airborne measurement made in the same period. The airborne measurements indicated alkene emissions of up to 50% higher than those of SOF measurements made at the same time, but considering the uncertainties of the estimates based on the airborne measurements this may not be unreasonable. If anything, the airborne measurements would indicate that the SOF measurements underestimate the discrepancies between inventory emissions and actual emissions.

4.2 Quantitative measurements and modeling of industrial formaldehyde emissions in the Greater Houston area during campaigns in 2009 and 2011

This paper investigates the occurrence of industrial sources of primary formaldehyde emissions in the Greater Houston area. The paper presents results from two measurement surveys using Mobile DOAS to detect and quantify local point sources of industrial formaldehyde emissions. The surveys were carried out in the largest conglomerates of refineries and petrochemical industries around Houston during measurement campaigns in 2009 and 2011. Five sources were repeatedly detected during the 2000 campaign, two in Texas City, two in Mont Belvieu and one in Houston Ship Channel. All except one of these were detected again during the 2011 campaign and two additional sources were found, one in Texas City and one in Houston Ship Channel. The average formaldehyde flux measured from these sources varied between 6 and 40 kg/h. The sum of the average emission measured from all sources was approximately 80 kg/h in 2009 and 130 kg/h in 2011. Since the surveys covered most large refineries and petrochemical facilities in the area, total primary formaldehyde emissions should not be expected to be drastically higher than these totals.

In 2009, ethene and propene emissions were measured with Solar Occultation Flux (SOF) in parallel to the Mobile DOAS measurements of formaldehyde during large parts of the survey. Thirteen cases were identified where the formaldehyde plume from one of these sources was detected together with a significant plume of ethene, propene or both. These were selected for investigation of whether the formaldehyde emissions could be explained by oxidation of the alkenes. For this purpose a Lagrangian photochemical plume model was used to simulate the plume chemistry for the thirteen cases. In addition to the ethene, propene and formaldehyde emissions, fluxes of alkanes measured with SOF, and

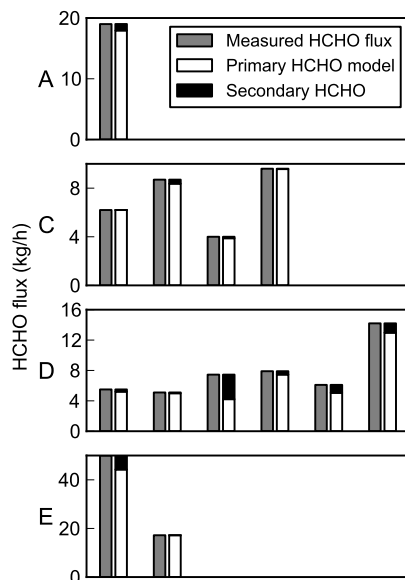


Figure 4.1: Measured HCHO fluxes for the 13 plume chemistry simulation cases and the fraction of it explained by primary and secondary emissions respectively according to the results. The cases are sorted by the emission source (labeled A, C, D and E) from which the plume was detected.

of NO_2 and SO_2 measured with Mobile DOAS were used as input data for the model in cases where they were detected. Measurement made at Moody Tower on the University of Houston campus as part of the SHARP campaign were also used as input. The results of the simulations are shown in figure 4.1. In one case, the plume chemistry model could assign as much as 43% of the formaldehyde flux to secondary emissions, but in most cases this fraction was lower than 10%.

A sensitivity analysis of the plume chemistry was performed to investigate which potential errors in the input data could have a meaningful effect on the outcome of the simulations. This showed that the parameters the model was most sensitive to were the wind speed, the vertical mixing speed and whether or not included alkane and NO_x were assumed to be coming from the same source as the formaldehyde and alkenes. Even with these parameters optimized for formaldehyde production within realistic constraints, the model could not explain more than a small fraction of the formaldehyde as secondary in most cases. From this it was concluded that most of the formaldehyde from the sources detected in these surveys was primary emissions. However, due to the large industrial emis-

sions of ethene and propene in the Houston area measured in these and other campaigns, secondary formaldehyde is still thought to dominate over primary emissions further downwind from emission sources.

4.3 Emission measurements of alkenes, alkanes, SO₂ and NO₂ from stationary sources in Southeast Texas over a 5-year-period using SOF and Mobile DOAS

In this paper results from SOF (Solar Occultation Flux) and Mobile DOAS measurements of industrial emissions of alkanes, alkenes (ethene and propene), SO₂ and NO₂ from four measurement campaigns in Southeast and East Texas are presented together to give an overview. The campaigns were carried out in four different years, 2006, 2009, 2011 and 2012, and partly overlapped in geographical coverage, mainly in that the three first studies were all heavily focused on the Greater Houston area. This allowed for comparisons between the different areas as well as from year to year. The largest difference from one year to another was seen in the alkene emissions from Houston Ship Channel (HSC). In 2006 the average ethene emission from HSC was approximately 1500 kg/h and propene emissions were almost 900 kg/h on average. In 2009 the same numbers had dropped to roughly 600 kg/h for both species and in 2011 the emissions remained on a similar level. Large variations were seen in the alkene fluxes measured from HSC in 2006, which suggests that the measurements were influenced by upset emissions. In that case the upset emissions could also be the explanation for the large difference between 2006 and 2009. Apart from this VOC emissions were surprisingly stable over the years. The alkane emissions from HSC, for instance, were within 10% of 11,500 kg/h during 2006, 2009 and 2011.

The measured emissions were all compared to reported annual average emissions for the corresponding areas. Emissions reported by the industries were extracted from the State of Texas Air Reporting System (STARS) and compiled by area and species. Measured alkane emissions were compared to reported emissions speciated as specific alkanes, unspecified alkanes, alcohols or broad categories that can be assumed to be dominated by alkanes, such as crude oil and naphtha. Ethene, propene and SO₂ could on the other hand be compared to their direct equivalent in the emission inventories. NO₂ was compared to emissions reported as either NO, NO₂ or NO_x, but NO_x was the most common speciation. According to airborne measurements during the 2006 campaign the typical NO₂ to NO_x ratio during the Mobile DOAS measurements was 0.75. In figure 4.2, the ratios between the average emission measured and the annual average emission reported have been calculated and plotted for each campaign, and for the areas and species that were measured in that campaign. This highlights the broad pattern that measured VOC emissions, both alkanes and alkenes, are typically

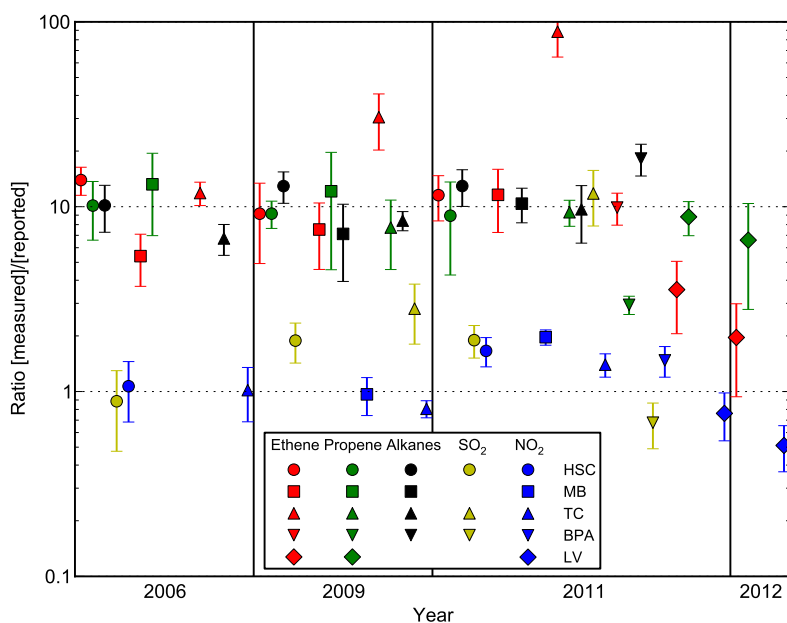


Figure 4.2: Ratios of emissions measured with SOF and Mobile DOAS to annual average emissions reported to State of Texas Air Reporting System (STARS) for each year, species and area. Circle markers are used for Houston Ship Channel (HSC), squares for Mont Belvieu (MB), upward triangles for Texas City (TC), downward triangles for Beaumont/Port Arthur (BPA) and diamonds for Longview (LV). Red markers are used for ethene, green for propene, black for alkanes, yellow for SO₂ and blue for NO₂. The markers indicate the ratio of the mean of all flux measurements to the reported emissions, while the error bars indicate ratio of the mean plus/minus one standard deviation to the reported emissions. The error bars only represent the variation in the flux measurements, not uncertainty in measurements or in reported emissions. The x-scale only indicates the year of the measurements; the x-position within a year has no meaning. Reported emissions for 2011 were used for the 2012 ratios since 2012 data was not yet available.

5–15 times larger than the corresponding reported emissions, while measured SO_2 and NO_2 emissions generally are closer to reported emissions, with typical ratios of 0.5–2. This pattern holds fairly well for most areas and years. It is argued that current methods for estimating emissions employed by industries might broadly underestimate the actual emissions for VOCs but not for SO_2 and NO_2 , due to larger uncertainties inherent to VOC emission mechanisms.

Additionally, the article investigates the possibility that measured VOC emission might be significantly unrepresentative of annual emissions due to the impact of the unrepresentative meteorological conditions during the measurements on evaporative losses. This is done by applying emission factor formulas from AP-42 to two example storage tanks, one external floating roof tank storing crude oil and one internal floating roof tank storing gasoline. These were chosen to represent the most common units in a refinery with significant meteorological effects in the emissions factor formulas. Emissions were estimated for these tanks using annual averages of temperatures, solar radiations and wind speeds measured in HSC as well as similar averages over just the campaign periods and over just the daytime hours in the days with measurements. Based on this, upper estimates of the effect of unrepresentative meteorological winds were in the interval 34–44% in all cases except the external floating roof tank during the 2011 campaign, in which the effect was estimated to be up to 90%. This was due to the exceptionally strong wind during that campaign which according to the emissions factor formulas has strong effects on external floating roof tanks. These effects are, however, too small to explain the discrepancies seen between measured and reported alkane emissions.

4.4 Mobile MAX-DOAS measurements of NO_2 and HCHO during the 2013 DISCOVER-AQ campaign in Houston

This paper presents an improved methodology to retrieve vertical tropospheric columns of NO_2 and HCHO from multi-axis (MAX-)DOAS measurement from a mobile platform. The method is applied to two days of measurements during a high ozone episode in the 2013 DISCOVER-AQ campaign in Houston. The purpose of the study was to evaluate the performance of optical remote sensing measurements of NO_2 and HCHO from high altitude aircraft, simulating measurements from a geostationary satellite. The methods that had been used previously to determine an offset term representing the column in the reference spectrum minus the stratospheric slant column was found to give unrealistic results and were therefor modified by incorporate radiative transfer modeling of the stratospheric slant column. Additionally, radiative transfer simulations were used to more accurately determine the air mass factors used to calculate the vertical tropospheric columns.

The vertical tropospheric columns derived from the mobile MAX-DOAS mea-

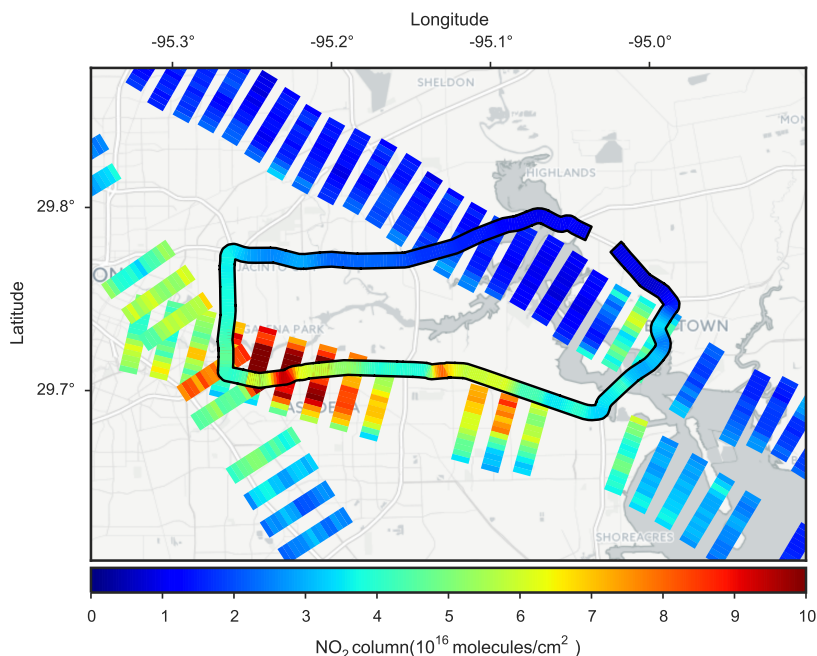


Figure 4.3: Tropospheric vertical columns of NO₂ in the Houston Ship Channel area determined from mobile MAX-DOAS measurements on September 25, 2013 shown on top of slant column measurements of NO₂ measured close in time by the nadir-viewing UV/visible spectrometer ACAM on board the NASA King Air airborne laboratory.

measurements were compared to measurements in the same area performed with a number of different methods used as a part of the DISCOVER-AQ campaign. Figure 4.3 shows a comparison with slant column measurements made from the NASA King Air airborne laboratory using the nadir-viewing UV/visible spectrometer Airborne Compact Atmospheric Mapper (ACAM). Unfortunately, the ACAM results have not yet been converted to vertical columns, but the slant columns show good qualitative spatial agreement with the mobile MAX-DOAS vertical columns and the quantitative discrepancies seem reasonable given the expected range of air mass factors for the ACAM. The mobile MAX-DOAS vertical columns were also compared to estimated columns based on in situ measurements from the NASA P3-B airborne laboratory which regularly flew in spiral patterns over a number of sites to measure vertical concentration profiles. These comparisons were limited by the lack of measurement coincidental in time, but among measurements within one hour time difference at the two sites closest to the mobile MAX-DOAS route the absolute average difference was $(27 \pm 27\%)$ for NO₂ columns and $(27 \pm 18\%)$ for HCHO columns. A third comparison was made with vertical NO₂ columns measured with the PANDORA direct-sun spectrom-

eters at the same sites that the P3-B flew in spirals over. For each passage of the mobile MAX-DOAS vehicle close to one of the sites, average vertical columns measured by both the PANDORA and the mobile MAX-DOAS were calculated and a linear relationship was fit to these data points for each site. Based on this, a systematic relative difference within 35% and a systematic absolute difference within $5 \cdot 10^{15}$ molecules/cm² were estimated.

5

Outlook

The research presented in this thesis has, together with previous work in the field, demonstrated the possibilities of quantifying industrial emissions by means of optical remote sensing methods. Even though these methods are fully operational today, there is plenty of room for improvements of the methods in the future, as well as to applying them to answer new questions.

One interesting development in recent years has been the surge of commercial wind lidars on the market. Accurately measuring elevated winds is difficult and it will continue to be crucial for almost any type of flux measurements in industrial emission plumes. No matter how accurate the measurements of columns or concentrations, it cannot compensate for uncertain wind measurements. If used properly, wind lidars seem to offer the perfect solution to this problem: continuous measurements of the wind velocity at several altitudes far above ground at high accuracy and time resolution. The only downside so far has been the cost. The use of wind lidars may already now be able to increase the accuracy of flux measurements. In the future fast 3D scanning lidars may be able to continuously scan the entire 3D wind velocity field downwind of an industry, which combined with column measurements downwind and a plume dispersion model may be able to make very accurate flux calculations as well as answer more detailed question about the plume dispersion. If not, we may at least experience wind lidars becoming the standard wind method for flux measurements.

Another interesting method development may be to further improve the mobile MAX-DOAS methodology that was presented in Paper IV. When designing that study this was a new method to us and there are several choices made for how to conduct the measurements which we may want to experiment with in future applications of this method, considering the lessons learned from the subsequent data analysis. For instance, we may want to try using different

viewing angles and combine multiple viewing directions in the subsequent data analysis. Another thing that could be beneficial is to regularly drive to rural unpolluted area to get a more stable offset determination.

In terms of future direction of research I think that one interesting path is to combine flux measurement methods more closely with chemistry and dispersion models, both to better understand what we are measuring and to in detail understand the effect of the emissions that we measure on photochemical smog and its impact on human air quality and the environment.

Bibliography

- [1] COSPAR International Reference Atmosphere (CIRA-86): Global Climatology of Atmospheric Parameters, January 2016.
- [2] Daniel J. Jacob. *Introduction to Atmospheric Chemistry*. Princeton University Press, 1999.
- [3] Frederick K. Lutgens and Edward J. Tarbuck. *The Atmosphere: An Introduction to Meteorology*. Prentice Hall, 2000.
- [4] WMO Greenhouse Gas Bulletin, 2015.
- [5] Anu Dudhia. Reference Forward Model (RFM) v4.34. <http://www.atm.ox.ac.uk/RFM/index.html>, October 2015.
- [6] Barbara J. Finlayson-Pitts and James N. Pitts Jr. *Chemistry of the Upper and Lower Atmosphere*. Academic Press, 2000.
- [7] F. Sherwood Rowland. Stratospheric ozone depletion. *Philosophical Transactions of the Royal Society of London B: Biological Sciences*, 361(1469):769–790, 2006.
- [8] IPCC. Climate Change 2014: Impacts, Adaptation, and Vulnerability. Part A: Global and Sectoral Aspects. Contribution of Working Group II to the Fifth Assessment Report of the Intergovernmental Panel on Climate Change, 2014.
- [9] K. N. Liou. *An Introduction to Atmospheric Radiation*. Academic Press, 2002.
- [10] Robert L. Kurucz. Compute spectra at various resolutions for models ASUN and ASUspectra. <http://kurucz.harvard.edu/sun.html>, 2005.
- [11] C. Fayt. *QDOAS 1.00*. Belgian Institute for Space Aeronomy, 1.00 edition, 2011.
- [12] Hayley Duffell, Clive Oppenheimer, and Mike Burton. Volcanic gas emission rates measured by solar occultation spectroscopy. *Geophysical Research Letters*, 28(16):3131–3134, 2001.

- [13] P. Weibring, J. Swartling, H. Edner, S. Svanberg, T. Caltabiano, D. Condarelli, G. Cecchi, and L. Pantani. Optical monitoring of volcanic sulphur dioxide emissions - comparison between four different remote-sensing spectroscopic techniques. *Optics and Lasers in Engineering*, 37(2 - 3):267 – 284, 2002.
- [14] Ibrahim Reda and Afshin Andreas. Solar position algorithm for solar radiation applications. *Solar Energy*, 76(5):577 – 589, 2004.
- [15] J. Mellqvist, B. Galle, T. Blumenstock, F. Hase, D. Yashcov, J. Notholt, B. Sen, J.-F. Blavier, G. C. Toon, and M. P. Chipperfield. Ground-based FTIR observations of chlorine activation and ozone depletion inside the Arctic vortex during the winter of 1999/2000. *Journal of Geophysical Research: Atmospheres*, 107(D20):SOL 6–1–SOL 6–16, 2002.
- [16] P. B. Fellgett. On the Ultimate Sensitivity and Practical Performance of Radiation Detectors. *J. Opt. Soc. Am.*, 39(11):970–976, Nov 1949.
- [17] A. A. Michelson and E. W. Morley. On the relative motion of the Earth and the luminiferous ether. *American Journal of Science*, Series 3 Vol. 34(203):333–345, 1887.
- [18] Peter R. Griffiths and James A. de Haseth. *Fourier Transform Infrared Spectroscopy*, volume 83 of *Chemical Analysis*. Wiley-Interscience, 1986.
- [19] Robert H. Norton and Reinhard Beer. New apodizing functions for Fourier spectrometry. *J. Opt. Soc. Am.*, 66(3):259–264, Mar 1976.
- [20] Manne Kihlman. *Application of Solar FTIR spectroscopy for quantifying gas emissions*. PhD thesis, Chalmers University of Technology, 2005.
- [21] J. K. E. Johansson, J. Mellqvist, J. Samuelsson, B. Offerle, B. Rappenglück, D. Anderson, B. Lefer, S. Alvarez, and J. Flynn. Quantification of industrial emissions of VOCs, NO₂ and SO₂ by SOF and Mobile DOAS. Technical Report 10-006, AQRP, 2011.
- [22] D. Perner, D. H. Ehhalt, H. W. Pätz, U. Platt, E. P. Röth, and A. Volz. OH - Radicals in the lower troposphere. *Geophysical Research Letters*, 3(8):466–468, 1976.
- [23] D. Perner and U. Platt. Detection of nitrous acid in the atmosphere by differential optical absorption. *Geophysical Research Letters*, 6(12):917–920, 1979.
- [24] U. Platt, D. Perner, and H. W. Pätz. Simultaneous measurement of atmospheric CH₂O, O₃, and NO₂ by differential optical absorption. *Journal of Geophysical Research: Oceans*, 84(C10):6329–6335, 1979.
- [25] Craig J. Sansonetti, Marc L. Salit, and Joseph Reader. Wavelengths of spectral lines in mercury pencil lamps. *Appl. Opt.*, 35(1):74–77, Jan 1996.

- [26] B. Galle, C. Oppenheimer, A. Geyer, A. J. S. McGonigle, M. Edmonds, and L. Horrocks. A miniaturised ultraviolet spectrometer for remote sensing of SO₂ fluxes: A new tool for volcano surveillance. *Journal of Volcanology and Geothermal Research*, 119(1-4):241–254, 2002.
- [27] C. Rivera, G. Sosa, H. Wöhrnschimmel, B. De Foy, M. Johansson, and B. Galle. Tula industrial complex (Mexico) emissions of SO₂ and NO₂ during the MCMA 2006 field campaign using a mobile mini-DOAS system. *Atmospheric Chemistry and Physics*, 9(17):6351–6361, 2009.
- [28] C. Rivera, J. Mellqvist, J. Samuelsson, B. Lefer, S. Alvarez, and M. R. Patel. Quantification of NO₂ and SO₂ emissions from the houston ship channel and texas city industrial areas during the 2006 texas air quality study. *Journal of Geophysical Research D: Atmospheres*, 115(8), 2010.
- [29] M. Johansson, B. Galle, T. Yu, L. Tang, D. Chen, H. Li, J. X. Li, and Y. Zhang. Quantification of total emission of air pollutants from Beijing using mobile mini-DOAS. *Atmospheric Environment*, 42(29):6926–6933, 2008.
- [30] M. Johansson, C. Rivera, B. DeFoy, W. Lei, J. Song, Y. Zhang, B. Galle, and L. Molina. Mobile mini-DOAS measurement of the outflow of NO₂ and HCHO from Mexico City. *Atmospheric Chemistry and Physics*, 9(15):5647–5653, 2009.
- [31] O. Ibrahim, R. Shaiganfar, R. Sinreich, T. Stein, U. Platt, and T. Wagner. Car MAX-DOAS measurements around entire cities: Quantification of NO_x emissions from the cities of Mannheim and Ludwigshafen (Germany). *Atmospheric Measurement Techniques*, 3(3):709–721, 2010.
- [32] T. Wagner, O. Ibrahim, R. Shaiganfar, and U. Platt. Mobile MAX-DOAS observations of tropospheric trace gases. *Atmospheric Measurement Techniques*, 3(1):129–140, 2010.
- [33] R. Shaiganfar, S. Beirle, M. Sharma, A. Chauhan, R. P. Singh, and T. Wagner. Estimation of NO_x emissions from Delhi using Car MAX-DOAS observations and comparison with OMI satellite data. *Atmospheric Chemistry and Physics*, 11(21):10871–10887, 2011.
- [34] G. Hönninger, C. von Friedeburg, and U. Platt. Multi axis differential optical absorption spectroscopy (MAX-DOAS). *Atmospheric Chemistry and Physics*, 4(1):231–254, 2004.
- [35] V.V. Rozanov, A.V. Rozanov, A.A. Kokhanovsky, and J.P. Burrows. Radiative transfer through terrestrial atmosphere and ocean: Software package {SCIATRAN}. *Journal of Quantitative Spectroscopy and Radiative Transfer*, 133:13 – 71, 2014.

- [36] John K. E. Johansson, Johan Mellqvist, Jerker Samuelsson, Brian Offerle, Barry Lefer, Bernhard Rappenglück, James Flynn, and Greg Yarwood. Emission measurements of alkenes, alkanes, SO₂, and NO₂ from stationary sources in Southeast Texas over a 5-yr period using SOF and mobile DOAS. *Journal of Geophysical Research: Atmospheres*, 119(4):1973–1991, 2014. 2013JD020485.
- [37] John K. E. Johansson, Johan Mellqvist, Jerker Samuelsson, Brian Offerle, Jana Moldanova, Bernhard Rappenglück, Barry Lefer, and James Flynn. Quantitative measurements and modeling of industrial formaldehyde emissions in the Greater Houston area during campaigns in 2009 and 2011. *Journal of Geophysical Research: Atmospheres*, 119(7):4303–4322, 2014. 2013JD020159.
- [38] C. Rivera, J. Mellqvist, J. Samuelsson, B. Lefer, S. Alvarez, and M. R. Patel. Quantification of NO₂ and SO₂ emissions from the Houston Ship Channel and Texas City industrial areas during the 2006 Texas Air Quality Study. *Journal of Geophysical Research D: Atmospheres*, 115(8), 2010.
- [39] David A. Smith, Michael Harris, Adrian S. Coffey, Torben Mikkelsen, Hans E. Jørgensen, Jakob Mann, and Régis Danielian. Wind lidar evaluation at the Danish wind test site in Høvsøre. *Wind Energy*, 9(1-2):87–93, 2006.
- [40] John U. White. Long Optical Paths of Large Aperture. *J. Opt. Soc. Am.*, 32(5):285–288, May 1942.
- [41] Steven W. Sharpe, Timothy J. Johnson, Robert L. Sams, Pamela M. Chu, George C. Rhoderick, and Patricia A. Johnson. Gas-Phase Databases for Quantitative Infrared Spectroscopy. *Applied Spectroscopy*, 58(12):1452–1461, 2004.
- [42] K. Bogumil, J. Orphal, T. Homann, S. Voigt, P. Spietz, O. C. Fleischmann, A. Vogel, M. Hartmann, H. Kromminga, H. Bovensmann, J. Frerick, and J. P. Burrows. Measurements of molecular absorption spectra with the SCIAMACHY pre-flight model: instrument characterization and reference data for atmospheric remote-sensing in the 230–2380 nm region. *Journal of Photochemistry and Photobiology A: Chemistry*, 157(2-3):167–184, 5/5/ 2003.
- [43] A. C. Vandaele, C. Hermans, P. C. Simon, M. Carleer, R. Colin, S. Fally, M. F. Mérienne, A. Jenouvrier, and B. Coquart. Measurements of the NO₂ absorption cross-section from 42 000 cm⁻¹ to 10 000 cm⁻¹ (238–1000 nm) at 220 K and 294 K. *Journal of Quantitative Spectroscopy and Radiative Transfer*, 59(3-5):171–184, 1998.

- [44] C. A. Cantrell, J. A. Davidson, A. H. McDaniel, R. E. Shetter, and J. G. Calvert. Temperature-dependent formaldehyde cross sections in the near-ultraviolet spectral region. *Journal of Physical Chemistry*, 94(10):3902–3908, 1990.
- [45] J. Mellqvist, J. K. E. Johansson, J. Samuelsson, B. Offerle, B. Rappenglück, C.-S. Wilmot, and R. Fuller. Investigation of VOC radical sources in the Houston area by the Solar Occultation Flux (SOF) method, mobile DOAS (SOF-II) and mobile extractive FTIR. Technical report, TERC, 2010.
- [46] J. Mellqvist, J. Samuelsson, C. Rivera, B. Lefer, and M. Patel. Measurements of industrial emissions of VOCs, NH₃, NO₂ and SO₂ in Texas using the Solar Occultation Flux method and mobile DOAS. Technical report, HARC, 2007.
- [47] S. C. Tucker, W. A. Brewer, R. M. Banta, C. J. Senff, S. P. Sandberg, D. C. Law, A. M. Weickmann, and R. M. Hardesty. Doppler lidar estimation of mixing height using turbulence, shear, and aerosol profiles. *Journal of Atmospheric and Oceanic Technology*, 26(4):673–688, 2009.

